Studies of spin relaxation and molecular dynamics in liquid crystals by two-dimensional Fourier transform electron spin resonance. I. Cholestane in butoxy benzylidene-octylaniline and dynamic cage effects

V. S. S. Sastry,[a] Antonino Polimeno,[b] Richard H. Crepeau, and Jack H. Freed
Baker Laboratory of Chemistry, Cornell University, Ithaca, New York 14853-1301

(Received 21 March 1996; accepted 24 May 1996)

Two-dimensional Fourier transform (2D-FT) electron spin resonance (ESR) studies on the rigid rodlike cholestane (CSL) spin-label in the liquid crystal solvent 4O,8 (butoxy benzylidene octylaniline) are reported. These experiments were performed over a wide temperature range: 96 °C to 25 °C covering the isotropic (I), nematic (N), smectic A (S_A), smectic B (S_B), and crystal (C) phases. It is shown that 2D-FT-ESR, especially in the form of 2D-ELDOR (two-dimensional electron–electron double resonance) provides greatly enhanced sensitivity to rotational dynamics than previous cw-ESR studies on this and related systems. This sensitivity is enhanced by obtaining a series of 2D-ELDOR spectra as a function of mixing time, T_m, yielding essentially a three-dimensional experiment. Advantage is taken of this sensitivity to study the applicability of the model of a slowly relaxing local structure (SRLS). In this model, a dynamic cage of solvent molecules, which relaxes on a slower time scale than the CSL solute, provides a local orienting potential in addition to that of the macroscopic aligning potential in the liquid crystalline phase. The theory of Polimeno and Freed for SRLS in the ESR slow motional regime is extended by utilizing the theory of Lee *et al.* to include 2D-FT-ESR experiments, and it serves as the basis for the analysis of the 2D-ELDOR experiments. It is shown that the SRLS model leads to significantly improved non-linear least squares fits to experiment over those obtained with the standard model of Brownian reorientation in a macroscopic aligning potential. This is most evident for the S_A phase, and the use of the SRLS model also removes the necessity of fitting with the unreasonably large CSL rotational asymmetries in the smectic phases that are required in both the cw-ESR and 2D-ELDOR fits with the standard model. The cage potential is found to vary from about k_BT in the isotropic phase to greater than $2k_BT$ in the N and S_A phases, with an abrupt drop to about $0.2k_BT$ in the S_B and C phases. Concomitant with this drop at the S_A–S_B transition is an almost comparable increase in the orienting potential associated with the macroscopic alignment. This is consistent with a freezing in of the smectic structure at this transition. The cage relaxation rate given by R^c, its ''rotational diffusion coefficient,'' is of order of 10^7 s^{-1} in the I and N phases. It drops somewhat in the S_A phase, but there is a greater than order of magnitude drop in R^c for the S_B and C phases to about 10^5 s^{-1}. This drop is also consistent with the freezing in of the smectic structure. The rotational diffusion tensor of the CSL probe is significantly larger than R^c which is consistent with the basic physical premise of the SRLS model. In particular, $R_\perp^o$ and $R_\parallel^o$ are of order 10^8 s^{-1} and 10^9 s^{-1} respectively. © *1996 American Institute of Physics.* [S0021-9606(96)51233-X]

I. INTRODUCTION

Two-dimensional Fourier transform (2D-FT) electron spin resonance (ESR)[1–3] has opened up the possibility of studying complex fluids with much greater resolution to structure and dynamics than hitherto possible by conventional cw-ESR methods,[4–6] the most powerful being the 2D-FT electron–electron double resonance (2D-ELDOR) experiment. In its 2D format it enables one to simultaneously distinguish homogeneous linewidths from inhomogeneous broadening and to measure the spin cross-relaxation rates. In viscous media where molecular motions are slowed down, one normally observes ''slow motional'' ESR spectra, which, in principle, can supply more detailed dynamic information, but they are usually broad and of low resolution. 2D-FT ESR in such cases also provides greatly enhanced resolution to the motional dynamics and the molecular ordering.[4–6] Recently, complex fluids, which display microscopic order but macroscopic disorder (MOMD), have been studied by 2D-ELDOR,[4,5] and it was shown that for such cases, wherein the MOMD leads to additional inhomogeneous broadening, the microscopic molecular ordering and the molecular rotational and translational dynamics could be studied to a much greater reliability than by conventional cw-ESR means.

Past cw-ESR studies of thermotropic liquid crystalline systems have had the advantage of macroscopic alignment of the sample, a phenomenon which occurs simply as a result of the alignment in a magnetic field, typically the field used for the ESR experiment. Considerable information has in the

[a]Permanent address: School of Physics, University of Hyderabad, Hyderabad 500 134, India.
[b]Permanent address: Department of Physical Chemistry, University of Padova, Via Loredan 2, 35131 Padova, Italy.

past been gleaned from such studies despite limited data from ESR linewidths in the motionally narrowed regime[7(a)] or from the ESR line shapes in the slow-motional regime.[7(b)] Nevertheless, these cw-ESR studies traditionally suffered from additional inhomogeneities such as those resulting from imperfections in sample alignment (i.e., sample mosaicity), and in an early application of 2D-FT-ESR[3] it was shown how this method readily overcomes such problems.

Given the enhanced resolution to structure and dynamics provided by 2D-ELDOR, one might inquire whether more detailed insights could be obtained by this method than previously by cw-ESR in the study of liquid crystals. For example, in liquid crystalline phases one must consider cooperative phenomena which can influence the rotational dynamics of the spin probe. The hydrodynamic model of order director fluctuations, which is important in nuclear magnetic relaxation (NMR) relaxation,[8] has been found to be too slow and too weak to contribute more than a small amount of inhomogeneous broadening in ESR.[7,9] Collective effects from critical and quasi-critical slowing of hydrodynamic modes near liquid–crystalline phase transitions have been found to be important in the molecular dynamics from ESR studies[10,11] and NMR studies.[12] Unlike the case for simple isotropic fluids, the motionally narrowed cw-ESR results for liquid crystals (away from the phase transitions) have typically exhibited linewidth anomalies for which a variety of mechanisms have been suggested.[7] Most useful has been a model of localized molecular cooperativity referred to as the slowly relaxing local structure (SRLS) model. In the SRLS model the slowly fluctuating components of the anisotropic intermolecular potential are regarded as a local structure, which persists for a mean time τ_c, that is much longer than the rotational correlation time, τ_R of the individual molecule. Simple approximate analyses of the effects of SRLS on motionally narrowed ESR spectra have met with moderate success,[7(a),9] but have also shown the limited information content available.

The early 2D-ELDOR study on a small spin-probe, perdeuterated Tempone, in the smectic A phase of the liquid crystal S2, illustrated how one could explore a more detailed dynamic model.[3] Since this probe is much smaller than the thickness of the smectic bilayer, a model involving rotational–translational coupling originally due to Moro and Nordio[13] was utilized. In this model a small probe is assumed to experience an orienting potential which depends upon its location in the smectic bilayer. Thus, as the spin probe translates through the smectic layer, its orientational potential is modulated. This model was useful in explaining the 2D-ELDOR cross-peaks and their angular dependence, but could not simultaneously explain the magnitude of the measured homogeneous T_2's and their (weak) angular dependence. (Here the angular dependence refers to the orientation of the nematic director with respect to the applied magnetic field for the macroscopically aligned sample.) More recent measurements of the anisotropic translational diffusion of this probe in the smectic phase of S2, have however been interpreted successfully in terms of such a model combined with a free-volume model.[14] We explore further the dynamics of the relatively small PD-Tempone probe over a range of liquid crystalline phases in the companion paper.[15]

In this paper we present a study by 2D-FT-ESR methods of the rotational relaxation of the relatively large and rigid cholestane probe with a shape that can be approximated as a cylinder with a length of 24 Å and a diameter of 6 Å.[16] It has been extensively used in past cw-ESR studies on rotational reorientation, and it has been found to typically yield slow-motional spectra in liquid crystalline phases.[7(b),17] However, in low temperature smectic phases, such as in 4O,8 solvent (which we use in the present study), the cw-ESR from CSL was found to show very little sensitivity to motional dynamics,[17] and spin-echo methods are required to properly distinguish the homogeneous linewidths for such cases.[18] Its length is nearly comparable to that of a smectic layer ($\sim$ 30 Å), and it is found to be a very good reporter of the overall or ''backbone'' molecular ordering within liquid crystalline phases. Also, the low concentration utilized hardly perturbs the phase behavior.[19] Studies of its anisotropic translational diffusion in the smectic phase of S2 were consistent with an absence of roto-translational coupling effects, as would be expected for a molecule of its size, since it simultaneously ''experiences'' the full length of a smectic bilayer.[14]

Our current objective was to explore the evidence for localized molecular cooperativity with this probe over a range of liquid crystalline phases using the latest capabilities in 2D-FT-ESR methodology. This probe had previously been employed in 2D-FT-ESR studies on membrane vesicles which exhibit the MOMD effect.[5] Whereas good agreement was found with theoretical predictions based on a simple model of rotational diffusion in a mean orienting potential, some systematic deviations were observed. It was felt that studies on well-aligned liquid crystalline phases would provide better and more resolved 2D-FT-ESR spectra with which to assess the possible role of localized dynamic cooperativity.

Since the CSL spectra in liquid crystalline phases is generally in the slow-motional regime, it is necessary to have a rigorous theory for the analysis of 2D-FT-ESR spectra in this regime. This has recently been accomplished for the standard model of rotational diffusion in an orienting potential (i.e., a rotational Smoluchowski equation).[4,6] The generalization of one-dimensional (1D) cw-ESR slow motional simulations to include the SRLS model, though complicated, has recently been achieved by Polimeno and Freed.[20] We present here the generalizations needed to include the SRLS model into the simulation of slow motional 2D-FT-ESR spectra. We again use the approach of globally fitting a set of 2D-ELDOR spectra as a function of mixing time by modern non-linear least squares methods in order to obtain optimum ordering and dynamic parameters from the very extensive data sets resulting from such experiments.[4,5,21] Thus the rapid calculation of theoretical spectra for the SRLS model is a practical necessity.

It is also important to note that our experimental format of obtaining the 2D-ELDOR spectra for 6–8 different mixing times actually presents a third dimension to the experiment. That is, the relative intensities and the shapes of the

auto and cross-peaks of a 2D-ELDOR spectrum may be observed as they change with mixing time. This is a source of the extensive spectral information that we find very useful to critically assess deviations from simple Markovian behavior in the molecular reorientation. In the presence of a dynamic cage, molecular reorientation is necessarily non-Markovian, so that this is an important feature of the experiment. In our theoretical analysis of the SRLS model we include both the usual Smoluchowski-type diffusive operator, which describes the rotation of the probe in a mean potential, and the diffusive operator for the rotation of the local structure (the cage) formed by the molecules in the immediate surroundings of the probe. As a result of the probe–cage interaction potential, neither the motion of the probe, nor that of the cage, can separately be regarded as Markovian processes. Instead, it is their collective motion which exhibits Markovian behavior in the form of a multi-dimensional Markov process.

The validity of a SRLS or cage-type model for fluids has recently received support from another source. In a molecular dynamics study of a simple diatomic molecular fluid, the use of a cage, defined in terms of the ensemble averaged instantaneous interaction potential of all molecules acting on a probe molecule, led to a stochastic model that was very effective in interpreting the results of the molecular dynamics calculation.[22] The SRLS cage model we use in this work is very similar to that stochastic model. In the present case for ESR, we are only interested in longer times, wherein inertial effects may be neglected, and we also allow for a macroscopic or mean orienting potential. Ultimately the relevance of the SRLS model must be judged on (i) the quality of the fits obtained versus those for the simpler standard model (or other models), and (ii) the extent to which the ordering and dynamic parameters obtained for the probe molecule and the cage are physically reasonable.

In Sec. II, we present experimental details. The theoretical approach used to include the SRLS model into the SLE method for simulating 2D-FT-ESR spectra is detailed in Sec. III. Our results are described in Sec. IV, and are further discussed in Sec. V. Conclusions appear in Sec. VI.

II. EXPERIMENTAL DETAILS

The liquid crystal *N*-(*p*-butoxybenzylidene)-*p*-*n*-octylaniline (4O,8) was prepared earlier in this laboratory, and the transition temperatures were confirmed by differential scanning calorimetry measurements as:

$$C \xrightarrow{34\ ^\circ\mathrm{C}} S_B \xrightarrow{48\ ^\circ\mathrm{C}} S_A \xrightarrow{62\ ^\circ\mathrm{C}} N \xrightarrow{77\ ^\circ\mathrm{C}} I. \tag{1}$$

The smectic layer spacing for 4O,8 is estimated to be about 28 Å from the value for 4O,7 of 26.8 Å obtained by x-ray measurements.[23] The nitroxide free radical 3′,3′-dimethyloxazolidinyl-*N*-oxy-2′, 3-5α-cholestane (CSL) was obtained from commercial sources. Solutions of CSL in 4O,8 at a concentration of about 4×10^{-3} M were prepared by mixing them very well for a prolonged period just above the clearing point. Samples were prepared in 2-mm-o.d. glass tubes after deoxygenating them with standard procedures and sealing them under vacuum.

ELDOR experiments were carried out on a home-built FT-ESR spectrometer,[2,24,25] as a function of temperature covering all the mesophases. These experiments used a $\pi/2 - t_1 - \pi/2 - T_m - \pi/2 - t_2$ pulse sequence. Similar experiments were also performed using the COSY sequence of $\pi/2 - t_1 - \pi/2 - t_2$. The width of the $\pi/2$ pulses typically was about 5 ns, which provides nearly uniform spectral rotation into the rotating $x-y$ plane over at least a $\pm$ 75 MHz bandwidth.[5,24,25] The signal after the last pulse was sampled every 1 ns, which is obtained by an interleaving method, and it yielded 256 data points. The separation between the first two pulses, or t_1, was stepped with 128 steps of 2 ns. The spectrometer dead time, τ_d was 60 ns, while the minimum separation between pulses was 50 ns. A 32 (8) step dual quadrature phase cycling sequence for 2D-ELDOR (COSY) provided the complex signal with respect to t_1 and t_2, and it provided for subtraction of all unwanted signals.[2,5,24,25] A full data collection required about 20 minutes for 2D-ELDOR. Each step in the phase cycling sequence was an average of 500 signals.

The sample temperature was regulated using a gas flow type cryostat with a commercial temperature controller (Bruker, model ER 4111 VT) to an accuracy of about ±1 °C. The magnetic field was stabilized using a standard field-frequency lock arrangement (Varian Fieldial, Mark II), leading to a typical field stability better than $\pm$ 10 mG (or about 3 parts in 10^6) during a 20 minute data collection. The microwave frequency was stabilized to an accuracy of about ±1 kHz (or about a part in 10^7) (using a Microwave Systems Inc., Model MOS lock box). Rotation of the sample director with respect to the static magnetic field is achieved by mounting the sample on a suitable goniometer.

In both the 2D ELDOR and COSY experiments the dual quadrature data were transformed to the S_{C-} combination for analysis. In all these cases there was no observable signal in the S_{C+} combination of the dual quadrature data. In the S_A and S_B phases these experiments were carried out as a function of the orientation of the director at two temperatures in each phase. The 2D-ELDOR measurements were performed for different ''mixing times'' T_m. Typically these spectra were recorded for at least six mixing times ranging from 90 to about 300–400 ns, the signal to noise ratio being the limiting factor for stepping out T_m further. The spectra showed no significant instrumental artifacts, and hence the time domain data were directly used, without any further processing, to generate 2D magnitude Fourier spectra.

The magnetic parameters of CSL in 4O,8 solvent have been given previously.[17] They are $A_{xx}=A_{yy}=5.27G, A_{zz}=33.44G; g_{xx}=2.0089, g_{yy}=2.0058, g_{zz}=2.0021$. For CSL the magnetic x-axis is along the N–O bond, and the magnetic z-axis is along the nitrogen $p-\pi$ orbital, with the magnetic y axis perpendicular to both. It is also known from the structure that the magnetic z-axis is parallel to the rotational y-axis, and the magnetic y-axis is tilted 15° with respect to the diffusional z-axis, leading to a corresponding tilt between

the magnetic x-axis and the diffusional x-axis.[20,26] (Traditionally one refers to the principal magnetic axes by x''', y''', and z''' and to the principal axes of rotational diffusion by x', y', and z').[7,9,10] Based upon molecular shape considerations, and standard practice, we take the principal axes of orientation of CSL to coincide with the x', y', and z' axes. Thus, except for the 15° tilt, CSL corresponds to a case of y-ordering, (i.e., the $y'''\|z'$).

III. THEORETICAL FRAMEWORK

A. The stochastic Liouville equation (SLE)

Let us consider a classical stochastic set of coordinates **Q**, which describe the motional degrees of freedom needed to represent the system. According to the stochastic Liouville approach, the density matrix $\rho(\mathbf{Q},t)$ is described semiclassically by the joint evolution of the internal quantum (spin) degrees of freedom and the classical motional dynamics:[27]

$$\frac{\partial}{\partial t}\hat{\rho}(\mathbf{Q},t) = -(\hat{\Gamma} + i\hat{\mathscr{H}}^{x})[\hat{\rho}(\mathbf{Q},t) - \hat{\rho}_0(\mathbf{Q})], \tag{2}$$

where $\hat{\mathscr{H}}^{x}$ is the quantum Liouville operator, i.e., the commutator superoperator associated with the spin Hamiltonian $\hat{\mathscr{H}}$ for the magnetic interactions, i.e.:

$$\hat{\mathscr{H}} = (\beta_e/\hbar)\mathbf{B_0}\cdot\mathbf{g}\cdot\mathbf{S} + \gamma_e\mathbf{I}\cdot\mathbf{A}\cdot\mathbf{S}, \tag{3}$$

where **g** and **A** are the g and hyperfine tensors, respectively, **S** and **I** are the electron spin and nuclear spin operators respectively, $\mathbf{B_0}$ is the dc magnetic field, β_e is the Bohr magnetron, γ_e, the electron gyromagnetic factor. In Eq. (2) $\hat{\Gamma}$ is a Markovian operator, usually a Smoluchowski or Fokker–Planck operator, describing the stochastic motion of the **Q** coordinates. The quantity $\hat{\Gamma} + i\hat{\mathscr{H}}^{x} = \hat{\mathscr{L}}$ is referred to as the stochastic Liouville operator (SLO). It is more convenient to use the reduced density operator $\hat{\chi}(\mathbf{Q},t) = \hat{\rho}(\mathbf{Q},t) - \hat{\rho}_0(\mathbf{Q})$, where $\hat{\rho}_0(\mathbf{Q})$ is the density matrix at thermal equilibrium:

$$\frac{\partial}{\partial t}\hat{\chi}(\mathbf{Q},t) = -\hat{\mathscr{L}}\hat{\chi}(\mathbf{Q},t). \tag{4}$$

The formal solution of Eq. (4) is naturally given by:

$$\chi(\mathbf{Q},t+t_0) = \exp(-\hat{\mathscr{L}}t)\chi(\mathbf{Q},t_0). \tag{5}$$

Equation (5) is solved numerically after diagonalizing a matrix representation of the SLO. Typically in the interpretation of ESR experiments in liquids, the phase space **Q** is limited to the Euler angles $\mathbf{\Omega}^o$ which specify the instantaneous orientation of the probe molecule with respect to an inertial frame (e.g., the laboratory frame or a fixed director frame for liquid crystals). The associated stochastic operator $\hat{\Gamma}(\mathbf{\Omega}^o)$ is usually chosen as a Smoluchowski operator, i.e., the spin probe is described as a Brownian rotator, in the presence of a static mean potential in the case of an ordered phase. In the SRLS model, the augmented phase space **Q** includes also the collective reorientation of the solvent structure in the form of a second set of Euler angles $\mathbf{\Omega}^c$. The SLE is then modified by replacing the diffusional operator $\hat{\Gamma}(\mathbf{\Omega}^o)$ with an augmented Smoluchowski operator $\hat{\Gamma}(\mathbf{\Omega}^o,\mathbf{\Omega}^c)$, which depends upon the interaction potential between the probe and the solvent structure or cage.[20]

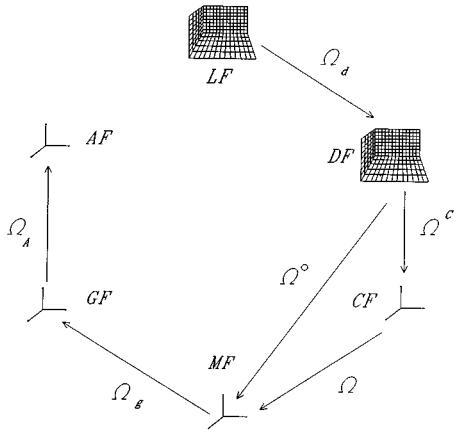

FIG. 1. Reference frames which define the structural and dynamic properties of the combined system of spin-bearing probe molecule and solvent cage: LF=lab frame, DF=director frame, MF=molecular frame, CF=cage frame, GF=g-tensor frame, AF=A-tensor frame.

The spin-dependent part of the SLO has been detailed in previous work by LBF and PF, [LBF=Ref. 6, and PF=Ref. 20]. When we consider the full SLO, we note that at least six different frames of references have to be introduced to clearly define the dynamic behavior of the spin probe *plus* cage system. They are the laboratory and director frames (LF and DF), which are inertial frames, and the molecular (MF), cage (CF), and the g and A tensor (GA and AF) frames, which are frames moving with the spin probe or in the case of the CF moving with the cage (see Fig. 1). The spin-Liouvillean can be written as the scalar operator which results from the scalar product of zero and second-rank irreducible spherical tensors and tensor operators; i.e., the $F^{(l,m)}_{\mu,L}$ which represent the relevant magnetic tensor components and the $A^{(l,m)}_{\mu,L}$ which represent the electron and nuclear spin operators in their irreducible tensor form (and the superscript x is used to denote the Liouville operator form):

$$\begin{aligned}\hat{\mathscr{H}}^{x} &= \sum_{\mu=g,A}\sum_{l=0,2}\sum_{m=-l}^{l} F^{(l,m)}_{\mu,L}{}^{*}\,\hat{A}^{(l,m)x}_{\mu,L} \\ &= \sum_{\mu=g,A}\sum_{l=0,2}\sum_{m=-l}^{l}\sum_{m'=-l}^{l}\sum_{m''=-l}^{l} \mathscr{D}^{l}_{mm'}(\mathbf{\Omega}_d) \\ &\quad\times \mathscr{D}^{l}_{m'm''}(\mathbf{\Omega}^o) F^{(l,m'')}_{\mu,M}{}^{*}\,\hat{A}^{(l,m)x}_{\mu,L}.\end{aligned} \tag{6}$$

Here $\mathbf{\Omega}_d$ specifies the orientation of the director frame relative to the laboratory frame. This spin Hamiltonian does not depend explicitly upon the solvent degrees of freedom, since the magnetic interaction terms are solely an internal property of the probe molecule. In Eq. (6) $X^{(l,m)}_{\mu,N}$ ($X=F,A$) stands for the mth component ($m=-l,\ldots,l$) in the N frame of the lth ($l=0,2$) rank irreducible spherical tensor or tensor operator, which relates to the interaction μ ($\mu=g$ or A); $\mathscr{D}^{l}_{mk}(\mathbf{\Omega})$ is a generic Wigner rotation matrix in $\mathbf{\Omega}$. The mo-

lecular components of the F tensors are defined in terms of their components in the proper magnetic frame. The components of the F and A tensor operators are summarized in LBF and PF.

The dynamical coupling between the probe and collective solvent modes for the SRLS model is contained in the two-body Smoluchowski operator:

$$\hat{\Gamma}=\hat{\mathbf{J}}^o\cdot R^o\cdot P_{\rm eq}\hat{\mathbf{J}}^o P_{\rm eq}^{-1}+\hat{\mathbf{J}}^c\cdot R^c\cdot P_{\rm eq}\hat{\mathbf{J}}^c P_{\rm eq}^{-1}. \tag{7}$$

Here $\hat{\mathbf{J}}^o$ is equal to the vector operator that generates an infinitesimal rotation of the probe (except for a factor $-i$), with components specified in the MF; $\hat{\mathbf{J}}^o$ is the equivalent operator for the cage, with components specified in the CF. The diffusional tensors R^o and R^c are time-independent and diagonal in the MF and in the CF, respectively. The Boltzmann distribution $P_{\rm eq}$ is defined with respect to a generic potential $V(\mathbf{\Omega}^o,\mathbf{\Omega}^c)$:

$$P_{\rm eq}(\mathbf{\Omega}^o,\mathbf{\Omega}^c)=\exp[-V(\mathbf{\Omega}^o,\mathbf{\Omega}^c)/k_BT]/\langle\exp[-V(\mathbf{\Omega}^o,\mathbf{\Omega}^c)/k_BT]\rangle \tag{8}$$

and

$$V(\mathbf{\Omega}^o,\mathbf{\Omega}^c)=V^o(\mathbf{\Omega}^o)+V^{\rm int}(\mathbf{\Omega}^o-\mathbf{\Omega}^c)+V^c(\mathbf{\Omega}^c). \tag{9}$$

As in PF the probe, cage, and interaction components of the potential displayed in Eq. (9) are explicitly defined in terms of second and fourth rank Wigner matrices as, respectively:

$$v^o(\mathbf{\Omega}^o)\equiv\frac{1}{k_BT}V^o(\mathbf{\Omega}^o)=-\sum_{l=2,4}\{a_0^l\,\mathscr{D}^l_{00}(\mathbf{\Omega}^o)+a_2^l[\,\mathscr{D}^l_{02}(\mathbf{\Omega}^o)+\mathscr{D}^l_{0-2}(\mathbf{\Omega}^o)]\}, \tag{10}$$

$$v^c(\mathbf{\Omega}^c)\equiv\frac{1}{k_BT}V^c(\mathbf{\Omega}^c)=-\sum_{l=2,4}\{b_0^l\,\mathscr{D}^l_{00}(\mathbf{\Omega}^c)+b_2^l[\,\mathscr{D}^l_{02}(\mathbf{\Omega}^c)+\mathscr{D}^l_{0-2}(\mathbf{\Omega}^c)]\}, \tag{11}$$

$$v^{\rm int}(\mathbf{\Omega})\equiv\frac{1}{k_BT}V^{\rm int}(\mathbf{\Omega})=-\sum_{l=2,4}\{c_0^l\,\mathscr{D}^l_{00}(\mathbf{\Omega})+c_2^l[\,\mathscr{D}^l_{02}(\mathbf{\Omega})+\mathscr{D}^l_{0-2}(\mathbf{\Omega})]\}. \tag{12}$$

Equations (10) and (11) correspond to the mean potentials experienced by the probe and the cage in a uniaxial liquid crystal, while for simplicity the potential of interaction of the probe in the cage, given by Eq. (12), is taken to also be uniaxial. (A brief discussion on more general potentials allowing for biaxial character of the cage is given in PF.)

In the course of a typical 2D-FT-ESR experiment, the system is subjected to a sequence of microwave pulses. The pulses are usually strong and approximately non-selective, i.e., they affect the spins over a wide frequency range.[6] Following LBF, we shall assume for simplicity that only ideal non-selective pulses are used. [Effects of imperfect coverage may be corrected for empirically as discussed elsewhere].[5] The evolution of the density matrix after a pulse of duration t_p is then given as:[6]

$$\rho(t_0+t_p)=\mathscr{P}\rho(t_0)=\hat{P}\rho(t_0)\hat{P}^{-1}. \tag{13}$$

Thus a complete formulation for interpreting a 2D-FT-ESR experiment requires the specification of the pulse propagator operator $\hat{P}$. This is given in LBF, in the absence of the cage, in terms of the matrix which acts on subsets of the set of basis vectors used to represent the SLO (see below). Here we shall generalize that expression to include the presence of the solvent degrees of freedom. However, we have first to define the complete set of basis vectors and to outline the computational procedure employed to evaluate actual 2D-ESR spectra.

B. Basis vectors

The generic basis set for representing $\hat{\mathscr{L}}$ and $\hat{P}$ is given by a direct product of spin operators and Wigner rotation matrices which span the space of the two sets of Euler angles, (i.e., $\mathbf{Q}=\mathbf{\Omega}^o,\mathbf{\Omega}^c$). Detailed descriptions are presented in PF and LBF, so only a brief summary is given here.

Basis states of the spin Hamiltonian for a single electron spin may be written as $|S,m_S\rangle$ in Hilbert space. Each ''spin-transition,'' which is an element of the basis for representing the spin superoperator $\hat{\mathscr{H}}^x$, can be characterized by the two transition numbers $p^S=m_S''-m_S'$ and $q^S=m_S''+m_S'$, where for the case of $S=1/2$ the values of $p^S=\pm1$ denote the two counter-rotating $x-y$ components of spin magnetization, and $p^S=0$ accounts for the z component. Similar quantum numbers p^I, q^I can be defined as the transition quantum numbers for the nuclear spin I. Thus in Liouville (transition) space the superoperator $\hat{\mathscr{H}}^x$ is spanned by the basis $|p^S,q^S,p^I,q^I\rangle\rangle$. The stochastic Liouville equation couples the spin system with the classical stochastic phase space $\mathbf{Q}$, so that a complete basis for representing $\hat{\mathscr{L}}$ is obtained by the direct product of the spin basis set and the complete set of basis functions which span the functional space $f(\mathbf{Q})$. In the case of the SRLS model, we use the direct product of Wigner rotation matrices for the two sets of Euler angles $\mathbf{\Omega}^o$ and $\mathbf{\Omega}^c$:

$$|p^S,q^S,p^I,q^I;L^o,M^o,K^o;L^c,M^c,K^c\rangle\rangle=|p^S,q^S,p^I,q^I\rangle\rangle\frac{[L^oL^c]^{1/2}}{8\pi^2}\times\mathscr{D}^{L^o}_{M^oK^o}{}^*(\mathbf{\Omega}^o)\,\mathscr{D}^{L^c}_{M^cK^c}{}^*(\mathbf{\Omega}^c). \tag{14}$$

In the following we shall let the cage potential, $V^c(\mathbf{\Omega}^c)$ of Eq. (11) be cylindrically symmetric. Then the symmetry of

the interaction potential between the probe and the cage, given by Eq. (12) will enable the neglect of the third cage quantum number K^c.[20]

In the high-field limit and when no microwave pulse is present, the stochastic Liouville matrix $\mathscr{L}$ is block-diagonal with respect to the coherence order of the electron spin, i.e., p^S. For $S=1/2$ we shall distinguish between the submatrices $\mathscr{L}_{\pm 1}$ (spanned by the off-diagonal subspaces $p^S=\pm 1$) and $\mathscr{L}_0$ (spanned by the diagonal space $p^S=0$). The three matrices can be diagonalized separately by different complex orthogonal transformations:

$$O_m^{\mathrm{tr}}\,\mathscr{L}O_m=\Lambda_m, \tag{15}$$

where $m=0,\pm 1$; O_m and Λ_m are, respectively, the eigenvectors and eigenvalues matrices for the mth subset. The diagonalization of each submatrix can be performed by using a suitable iterative algorithm like the Lanczos or the conjugate gradient[27,28] algorithm.

The pulse propagator $\hat{P}$ is still to be defined. For a particular coherence pathway we may write $P_{(p_1^S\leftarrow p_2^S)}$ as the corresponding pulse propagator, where p_1^S and p_2^S are the coherence orders after and before the pulse, respectively. Each such pulse propagator is proportional to the unit matrix spanning the associated sub-space(s) of the matrix representation of the SLE. Each non-zero element shows a typical dependence on the phase of the pulse, which we may write as $\langle\langle p_1^S|P\,|p_2^S\rangle\rangle \propto \exp[-i(p_1^S-p_2^S)\phi]$.[6] This provides the basis for the selection of the coherence pathway by phase cycling. The 2D-ESR signal for a particular experiment may be written down quite simply once (i) the matrix representation in the diagonal and off-diagonal subspaces of the operator is obtained, (ii) the matrix representation of the pulse propagator to switch between the sets of subspaces is obtained (from Eq. (11) of LBF); and (iii) the eigenvalues and eigenvectors of the SLE are found. For example, the *FID* signal can be written as:[6]

$$S^{FID}\propto \langle\langle v_{-1}|O_{-1}\exp(-\Lambda_{-1}t_1)O_{-1}^{\mathrm{tr}}\,|v_{-1}\rangle\rangle, \tag{16}$$

where $P_{(\pm 1\leftarrow 0)}\rho_0$ is the density matrix after the first $\pi/2$ pulse. The two-pulse COSY $S_{c\pm}$ signals have coherence pathways $p^S=0\rightarrow\pm 1\rightarrow -1$; they are written as:

$$\begin{aligned}S_{c_{\pm 1}}^{\mathrm{COSY}}\propto\ &\langle\langle v_{-1}|O_{-1}\exp(-\Lambda_{-1}t_2)O_{-1}^{\mathrm{tr}}P_{(-1\leftarrow\mp 1)}O_{\mp 1}\\ &\times\exp(-\Lambda_{\mp 1}t_1)O_{\mp 1}^{\mathrm{tr}}\,|v_{\mp 1}\rangle\rangle.\end{aligned} \tag{17}$$

The ELDOR $S_{c_{\pm 1}}$ signals with coherence pathway $p^S=0\rightarrow\mp 1\rightarrow 0\rightarrow -1$ are given by:

$$\begin{aligned}S_{c_{\pm 1}}^{\mathrm{ELDOR}}\propto\ &\langle\langle v_{-1}|O_{-1}\exp(-\Lambda_{-1}t_2)O_{-1}^{\mathrm{tr}}P_{(-1\leftarrow 0)}O_0\\ &\times\exp(-\Lambda_0 T_m)O_0^{\mathrm{tr}}P_{(0\leftarrow\mp 1)}O_{\mp 1}\\ &\times\exp(-\Lambda_{\mp 1}t_1)O_{\mp 1}^{\mathrm{tr}}\,|v_{\pm 1}\rangle\rangle.\end{aligned} \tag{18}$$

The COSY signals are formally equivalent to the ELDOR signals for zero mixing times, i.e., $T_m=0$.

C. Matrix elements

Following Meirovitch *et al.*,[29] we write the matrix elements of the SLE $\hat{\mathscr{H}}^x$ operator in the (as yet unsymmetrized) basis set after making appropriate changes to take account of the presence of the cage:[20]

$$\begin{aligned}\langle\langle\mathbf{\Sigma}_1|\hat{\mathscr{H}}^x|\mathbf{\Sigma}_2\rangle\rangle=\ &\delta_{L_1^c,L_2^c}\delta_{M_1^c,M_2^c}[L_1^oL_2^o]^{1/2}\\ &\times\sum_{\mu=g,A}\sum_{l=0,2}\sum_{m=-l}^{l}\sum_{m'=-l}^{l}\sum_{m''=-l}^{l}\mathscr{D}_{mm'}^{l}\\ &\times(\mathbf{\Omega}_d)\begin{pmatrix}L_1^o & l & L_2^o\\ M_1^o & M_2^o-M_1^o & -M_2^o\end{pmatrix}\\ &\times\begin{pmatrix}L_1^o & l & L_2^o\\ K_1^o & K_2^o-K_1^o & -K_2^o\end{pmatrix}F_{\mu,M}^{(l,m'')*}\\ &\times\langle\langle\boldsymbol{\sigma}_1|\hat{A}_{\mu,L}^{(l,m)}|\boldsymbol{\sigma}_2\rangle\rangle,\end{aligned} \tag{19}$$

where the effect of the spin operators is concentrated in the last factor, which contains the reduced matrix elements that depend only upon the spin part of the basis set. The reduced matrix elements are given, for example, in PF. Here $|\mathbf{\Sigma}\rangle\rangle$ and $|\boldsymbol{\sigma}\rangle\rangle$ respectively represent the complete set of quantum numbers and just the subset of magnetic quantum numbers. Detailed expressions of the F and A tensors, for the hyperfine tensor ($\mu=A$) and electronic g-tensor ($\mu=g$) are given, for example in PF. The indices M and L are referred to the MF and LF, where the F and A tensors respectively are naturally defined.

The symmetrized diffusional operator $\tilde{\Gamma}=P_{\mathrm{eq}}^{-1/2}\hat{\Gamma}P_{\mathrm{eq}}^{1/2}$ has a more complicated matrix representation.[20] It is convenient to split the operator into four distinct contributions:

$$\tilde{\Gamma}=\tilde{\Gamma}^{\mathrm{sym}}+\tilde{\Gamma}^{\mathrm{asym}}+F^{\mathrm{sym}}+F^{\mathrm{asym}}. \tag{20}$$

The first two terms do not depend upon the potential; the axially symmetric term is:

$$\tilde{\Gamma}^{\mathrm{sym}}=R_\perp^o\hat{\mathbf{J}}^{o2}+(R_\parallel^o-R_\perp^o)\hat{J}_z^{o2}+R^c\hat{\mathbf{J}}^{c2}. \tag{21}$$

Here we are assuming an isotropic diffusion tensor for the cage, $R^c=R^c\mathbf{1}$ for simplicity, (or more precisely, R^c may be replaced by $R_\perp^c$ for an axially symmetric diffusion tensor).[6] The asymmetric term is:

$$\tilde{\Gamma}^{\mathrm{asym}}=R_d^o(\hat{J}_x^{o2}-\hat{J}_y^{o2}), \tag{22}$$

where

$$R_\perp^o=\frac{R_x^o+R_y^o}{2}, \tag{23}$$

$$R_\parallel^o=R_z^o, \tag{24}$$

$$R_d^o=\frac{R_x^o-R_y^o}{4} \tag{25}$$

and R_x^o, R_y^o, and R_z^o are the 3 principal components of the rotational diffusion tensor for the probe expressed in the molecular frame (MF) in which this tensor is diagonal. Since $\tilde{\Gamma}$ is independent of the spin degrees of freedom, we have:

$$\langle\langle \mathbf{\Sigma}_1|\widetilde{\Gamma}|\mathbf{\Sigma}_2\rangle\rangle = \delta_{\boldsymbol{\sigma}_1,\boldsymbol{\sigma}_2}\langle \boldsymbol{\lambda}_1|\widetilde{\Gamma}|\boldsymbol{\lambda}_2\rangle, \tag{26}$$

where $|\boldsymbol{\lambda}\rangle = |L^o M^o K^o L^c M^c\rangle$. The matrix element of $\widetilde{\Gamma}^{\rm sym}$ and $\widetilde{\Gamma}^{\rm asym}$ are readily evaluated:

$$\langle \boldsymbol{\lambda}_1|\widetilde{\Gamma}^{\rm sym}|\boldsymbol{\lambda}_2\rangle = \delta_{\boldsymbol{\lambda}_1,\boldsymbol{\lambda}_2}[R_\perp^o L^o(L^o+1) + (R_\parallel^o - R_\perp^o)K^{o2} + R^c L^c(L^c+1)], \tag{27}$$

$$\langle \boldsymbol{\lambda}_1|\widetilde{\Gamma}^{\rm asym}|\boldsymbol{\lambda}_2\rangle = \delta_{L_1^o,L_2^o}\delta_{M_1^o,M_2^o}\delta_{L_1^c,L_2^c}\delta_{M_1^c,M_2^c} \times \frac{R_d^o}{2}[c^-_{L_2^o K_2^o} c^-_{L_2^o K_2^o - 1}\delta_{K_1^o,K_2^o-2} + c^+_{L_2^o K_2^o} c^+_{L_2^o K_2^o+1}\delta_{K_1^o,K_2^o+2}]. \tag{28}$$

The functions $F^{\rm sym}$ and $F^{\rm asym}$ can be written in the form of an expansion of probe–cage normalized Wigner functions:

$$V(\mathbf{\Omega}^o,\mathbf{\Omega}^c) = \sum_{\boldsymbol{\lambda}} v_{\boldsymbol{\lambda}}|\boldsymbol{\lambda}\rangle, \tag{29}$$

$$F^{\rm sym}(\mathbf{\Omega}^o,\mathbf{\Omega}^c) = \sum_{\boldsymbol{\lambda}} f^{\rm sym}_{\boldsymbol{\lambda}}|\boldsymbol{\lambda}\rangle, \tag{30}$$

$$F^{\rm asym}(\mathbf{\Omega}^o,\mathbf{\Omega}^c) = \sum_{\boldsymbol{\lambda}} f^{\rm asym}_{\boldsymbol{\lambda}}|\boldsymbol{\lambda}\rangle. \tag{31}$$

The $v_{\boldsymbol{\lambda}}$ parameters are easily related to the natural potential parameters a_m^l, b_m^l, and c_m^l in Eqs. (10)–(12), respectively; the $f_{\boldsymbol{\lambda}}$ are calculated in terms of complicated sums of the $v_{\boldsymbol{\lambda}}$.[20] The matrix elements are completely defined once the integral of three $|\boldsymbol{\lambda}\rangle$ functions is explicitly written in terms of products of integrals of Wigner rotation matrices.[20]

Following LBF, additional relaxation terms have been included in the 2D-ESR formulation which were not present in the previous cw work of PF, namely: (i) the Heisenberg spin exchange contribution $\widetilde{\Gamma}_{\rm ex}$, whose magnitude is measured by the Heisenberg frequency $\omega_{\rm HE}$; (ii) the rotationally independent electron spin flip term, $\widetilde{\Gamma}_{W_e}$, measured by the electron spin flip rate W_e; and (iii) the rotationally independent nuclear spin flip term, $\widetilde{\Gamma}_{W_n}$, measured by the nuclear spin flip rate W_n. These terms are basically the same in the presence or in the absence of the SRLS, since they do not depend upon $\mathbf{\Omega}^c$; explicit expressions are given by LBF.

The symmetry properties of the SLE may be exploited by representing the operator in a new basis set which is a linear combination of unsymmetrized basis functions. The K-symmetrization and M_T-symmetrization for the SRLS problem have been already discussed by PF. The K-symmetrized basis set is given as:

$$|p^S q^S p^I q^I; L^o M^o K^o j^K L^c M^c\rangle\rangle_K = \mathcal{N}^K[|L^o M^o K^o L^c M^c K^c p^S q^S p^I q^I\rangle\rangle + j^K s^K|L^o M^o - K^o L^c M^c K^c p^S q^S p^I q^I\rangle\rangle], \tag{32}$$

where

$$s^K = (-)^{L^o+K^o}, \tag{33}$$

$$\mathcal{N}^K = [2(1+\delta_{K^o,0})]^{-1/2} \tag{34}$$

and now K is a non-negative number, where

$$\text{for } K^o = 0, \quad j^K = (-)^{L^o}, \qquad \text{for } 0 < K^o \leqslant L^o, \quad j^K = \pm 1. \tag{35}$$

Symmetrization with respect to M^o, M^c and p^I, which is included in order to exploit the symmetry properties of the Liouvillean at high field values, is substantially different from the standard ''M-symmetrization'' which was used in the past (LBF), for the case of a single Brownian rotator. We shall refer to the present, more general case, as M_T-symmetrization, where $M_T = M^o + M^c$ is the projection quantum number relative to the LF $z-$axis of the *total* ''angular momentum'' (i.e., probe plus cage ''angular momentum''):

$$|p^S q^S p^I q^I; L^o M^o K^o j^K L^c M^c j\rangle\rangle_M = \mathcal{N}^M[|p^S q^S p^I q^I; L^o M^o K^o j^K L^c M^c j\rangle\rangle + js|p^S - q^S - p^I q^I; L^o - M^o K^o j^K L^c - M^c\rangle\rangle], \tag{36}$$

where the following quantities are defined:

$$s^S = (-)^{L^o+L^c+M^o+M^c+q^S}, \tag{37}$$

$$\mathcal{N}^M = [2(1+\delta_{M^o,0}\delta_{M^c,0}\delta_{p^I,0}\delta_{q^S,0})]^{-1/2}, \tag{38}$$

and $j = (-)^{L^o+L^c}$ when $p^I = M^c = M^o = q^S = 0$, and is equal to ± 1 for all other allowed combinations of these four quantum numbers (cf. PF). (When $M^0 = 0$, then this reduces to the standard ''M-symmetrization.'') The SLE matrix elements in the symmetrized basis set are easily related to the unsymmetrized ones as expressed in PF.

The starting vector element in the symmetrized basis set is simply related to the unsymmetrized basis set representation of the Boltzmann distribution of Eq. (8). We associate the cw-ESR spectrum with the spectral density related to the x-component in the LF of the electronic magnetization, so that the appropriate starting vector is proportional to $\hat{S}_\pm$:

$$|v_\pm\rangle\rangle = [I]^{-1/2}|\hat{S}_\pm \otimes \mathbf{1}_I \otimes P_{\rm eq}^{1/2}\rangle\rangle, \tag{39}$$

where $\mathbf{1}_I$ is the unit operator in the nuclear spin space. The starting vector generic element in the symmetrized basis set is then given by:

$$\langle\langle \mathbf{\Sigma}|v_{\pm}\rangle\rangle = \mathcal{N}\delta_{p^I,0}\delta_{|p^S|,1}(1+j^K)(1+j)\langle\boldsymbol{\lambda}|P_{\mathrm{eq}}^{1/2}\rangle, \quad (40)$$

where $\mathcal{N}$ is the normalization for the fully symmetrized (K^o and M_T symmetrization) basis set (cf. PF). The reduced vector element $p_{\boldsymbol{\lambda}}=\langle\boldsymbol{\lambda}|P_{\mathrm{eq}}^{1/2}\rangle$ can be evaluated by factoring the equilibrium distribution, and then using the completeness of the $|\boldsymbol{\lambda}\rangle$ space (cf. PF).

Finally, we need to find an explicit expression for the pulse propagators in the symmetrized basis. The task is a straightforward generalization of the formulas presented by LBF. The pulse propagator for the conversion from the off-diagonal space into the diagonal space is then given as:

$$\begin{aligned} P_{(0\leftarrow\pm1)}|\pm1,0,p^I,q^I;L^oM^oK^oj^KL^cM^cj\rangle\rangle_M \\ = \pm(1+\delta_{p^I,0}\delta_{M^o,0}\delta_{M^c,0})^{-1/2} \\ \times[|0,1,p^I,q^I;L^oM^oK^oj^KL^cM^cj\rangle\rangle_M \\ + j(-)^{L^o+L^c+M^o+M^c} \\ \times|0,-1,-p^I,q^I;L^o-M^oK^oj^KL^c-M^cj\rangle\rangle_M] \end{aligned} \quad (41)$$

while the pulse propagator for the conversion from the diagonal space into the off-diagonal space is:

$$P_{(\pm1\leftarrow0)}|0,1,p^I,q^I;L^oM^oK^oj^KL^cM^cj\rangle\rangle_M = \begin{cases} (1+\delta_{p^I,0}\delta_{M^o,0}\delta_{M^c,0})^{1/2}(|1,0,p^I,q^I;L^oM^oK^oj^KL^cM^cj\rangle\rangle_M \\ \quad -|-1,0,p^I,q^I;L^oM^oK^oj^KL^cM^cj\rangle\rangle_M), \quad M^o\geqslant 0 \\ j(-)^{L^o+L^c+M^o+M^c}(|1,0,-p^I,q^I;L^o-M^oK^oj^KL^c-M^cj\rangle\rangle_M \\ \quad -|-1,0,-p^I,q^I;L^o-M^oK^oj^KL^c-M^cj\rangle\rangle_M), \quad M^o<0. \end{cases} \quad (42)$$

The pulse propagator from the $p^S=1$ space into the $p^S=-1$ space, which appears in the COSY experiment, is again a unit matrix.

D. Basis sets

The problem of calculating the 2D-FT-ESR spectrum is thus reduced to the diagonalization of the two complex symmetric matrices in the diagonal and off-diagonal subspaces. The necessity of calculating the eigenvectors as well as the eigenvalues is the main source of the additional computational effort that is required in the 2D-FT case with respect to cw ESR, where eigenvalues are required, but only the projections of the eigenvectors on the starting vector are needed. The Lanczos algorithm[27,28] can be used to first tridiagonalize the matrices; next the QR algorithm[6,27,28] is employed to find the eigenvalues. The eigenvectors corresponding to dominant eigenvalues are found by inverse iteration.

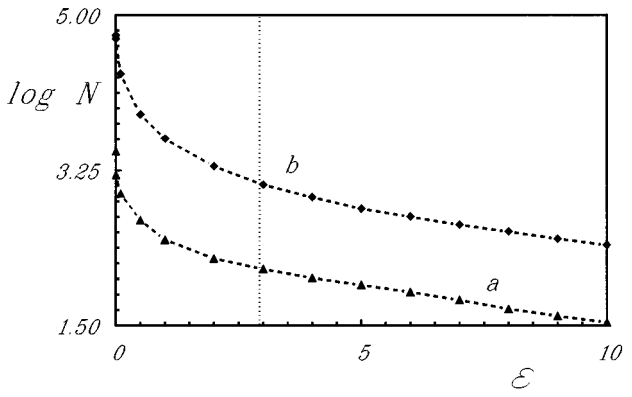

FIG. 2. Logarithm of the dimension of the pruned basis set as a function of the percentage tolerance, ϵ. Curve a is for the PDT case; curve b is for the CSL case.

The dimensions of the matrices which must be handled are quite large. Due to the presence of two additional quantum numbers, L^c, M^c, the computational effort, compared to the traditional single-body Smoluchowski approach, is definitely increased. However, symmetries contribute to keep the number of basis functions to a manageable number. First of all, only even values of L^c are included, due to the absence of odd rank Wigner functions in the cage potential. Second, in the absence of director tilt, the projection numbers along the LF z-axis obey the selection rule $M^o+M^c=p^I$: the resulting reduction in the dimension of the basis set amounts to at least a factor of 10. Still the dimensions of the matrices which have to be diagonalized are respectable [up to $N\approx O(10^5)$ for a typical slow-motion spectrum with $R^o\geqslant 10^7\ \mathrm{s}^{-1}$ and $R^c\geqslant 10^6\ \mathrm{s}^{-1}$].

However, one can determine a minimum set of basis vectors by using the ''pruning'' technique described by Vasavada *et al.*[30] This technique is based on the idea that only a subset of the original basis vectors is actually needed for a satisfactory (within a given percentage error, ϵ) agreement with experiment. First the solution vector of the related cw-ESR problem is found. Since each element in the solution vector is a measure of the relevance of the corresponding basis vector in representing the cw-ESR spectrum at each sweep-field position, one can perform this analysis for a number of field sweep positions and retain all the basis functions whose projection on to the normalized solution vector is greater than a given tolerance (usually $\epsilon=3\%$ is enough to assure a sensible agreement).

Once the minimum required basis set is obtained, a systematic comparison between the experimental 2D spectrum and the simulation is performed until the best fitting set of parameters (potential coefficients, probe diffusion and cage diffusion coefficients) is obtained. Following Lee *et al.*,[6,21] a non-linear least square fitting criterion, which is based on the

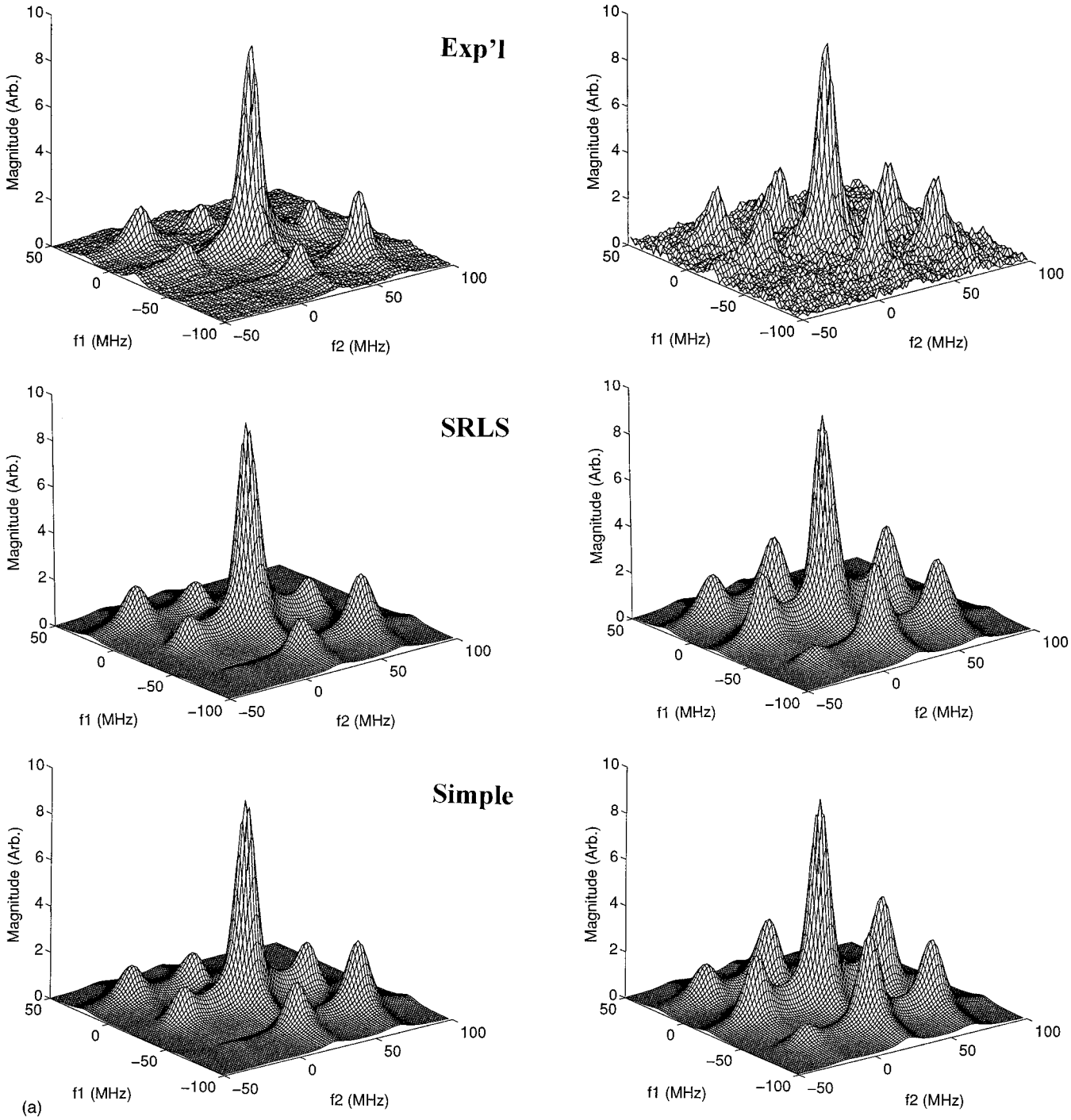

FIG. 3. Comparison of experimental and simulated 2D-ELDOR spectra (stack plots), based on SRLS and standard models, at representative temperatures in each phase: (a) isotropic, 91 °C; (b) nematic, 66 °C; (c) smectic A, 59 °C; (d) smectic B, 41 °C; (e) crystal, 29 °C. Left (right) column is for T_m=90 ns (250) in (a), 90 ns (200 ns) in (b), 110 ns (250 ns) in (c), 200 ns (300 ns) in (d), and 200 ns (400 ns) in (e). Top spectra are experimental, middle spectra are SRLS simulations, bottom spectra in (a), (b), and (c) are standard simulations. (a) is shown above, and Figs. (b)–(e) are shown on subsequent pages.

Marquardt–Levenberg procedure, has been used in the cases considered in this work.

Two sets of simulations for paramagnetic probes dissolved in an ordered phase have been performed. The first set was used in the study of PDT dissolved in 4O,8 (cf. Ref. 15). The motional rates in that case are relatively large since $R^o \approx 10^{10}$ s^{-1} and $R^c \approx 10^8$ s^{-1}. The potential coefficients, both for the probe and interaction potentials, were determined in the range of 1–2 k_BT. The basis set employed for these calculations was selected by starting with truncation values $L^o_{\max}=8$, $M^o_{\max}=4$, $K^o_{\max}=4$, $L^c_{\max}=6$, $M^c_{max}=6$; before pruning, this corresponds to a total number of 2960 functions for the off-diagonal subspace (note that this is the dimension after applying the selection rule $M^o+M^c=p^I$).

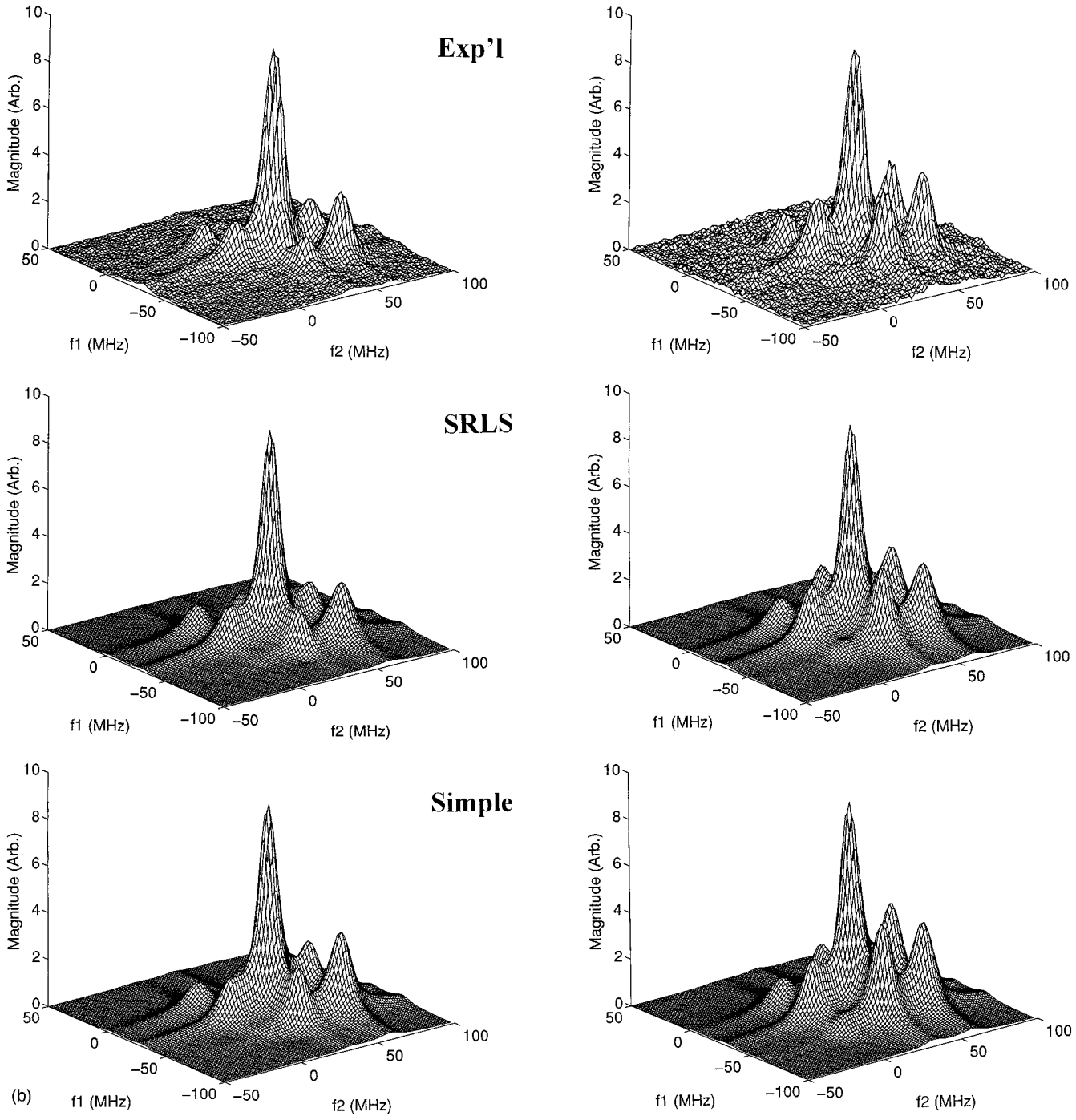

FIG. 3(b). See caption to Fig. 3(a).

After pruning (with a 3% tolerance) one obtains a reduced set of 139 functions.

The large reduction is mainly due to the curbing of the quantum numbers related to the cage, L^c and M^c. As a result of the pruning, L^c values larger than 4 were discarded and M^c values were limited to be between 2 and -4. Such large reductions in the dimensions of the pruned basis sets are partially due to an overestimation in the size of the initial basis set. We show in Fig. 2(a) how the logarithm of the dimension of the pruned basis set depends on the tolerance. With a severe 0.05% tolerance, the basis dimension is nevertheless reduced to 1204. The dotted vertical line marks the 3% value.

Notice that after pruning (with a 3% tolerance), the minimum truncation scheme (MTS) is given by $L^o_{\max}=6$, $M^o_{\max}=K^o_{\max}=4$, $-1\leqslant p^I\leqslant 2$, $L^c_{\max}=4$, and $-4\leqslant M^c\leqslant 2$. Prior to pruning, this MTS (but with $|p^I|\leqslant 2$ and $|M^c|\leqslant 4$) corresponds to 1262 functions, which is significantly larger than the pruned basis set of 297 functions.

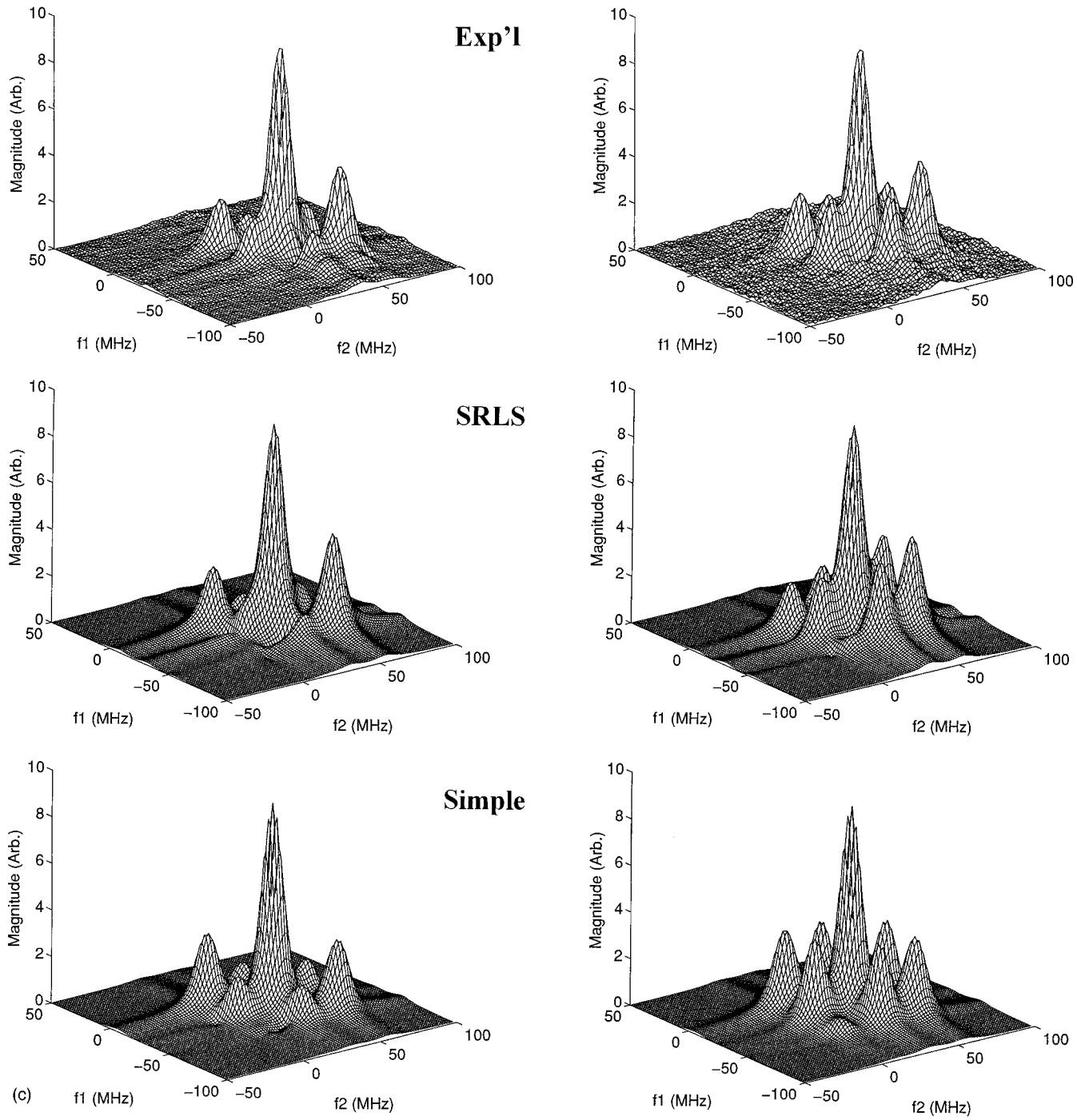

FIG. 3(c). See caption to Fig. 3(a).

The second set of simulations were performed in the present study of CSL dissolved in 4O,8. Since CSL is much larger than PDT, the motional rates are lower, $R_{\perp}^{o} \approx 10^{8}\ \mathrm{s}^{-1}$ and $R^{c} \approx 10^{7} - 10^{5}\ \mathrm{s}^{-1}$. Also the potential coefficients are in the range of $2k_BT$. Consequently, a significantly larger basis set had to be used. Initial truncation values chosen were $L_{\max}^{o}=18$, $M_{\max}^{o}=12$, $K_{\max}^{o}=12$, $L_{\max}^{c}=12$, $M^{c}=12$. Before pruning this corresponds to a total of 58 884 functions for the off-diagonal space. After pruning (with a 3% tolerance) it was reduced to just 1252 functions. (For a 1% tolerance the pruned set is made up of 4091 functions.) After pruning (3% tolerance), the MTS was found to be $L_{\max}^{o}=14$, $M_{\max}^{o}=6$, $K_{\max}^{o}=10$, $-1 \leqslant p^{I} \leqslant 2$, $L_{\max}^{c}=10$, $-6 \leqslant M^{c} \leqslant 2$. Prior to pruning, this MTS (but with $|p^{I}| \leqslant 2$ and $|M^{c}| \leqslant 6$) corresponds to 22 623 functions. Figure 2(b) shows the reduction of the pruned basis set dimension with increasing tolerance for this case.

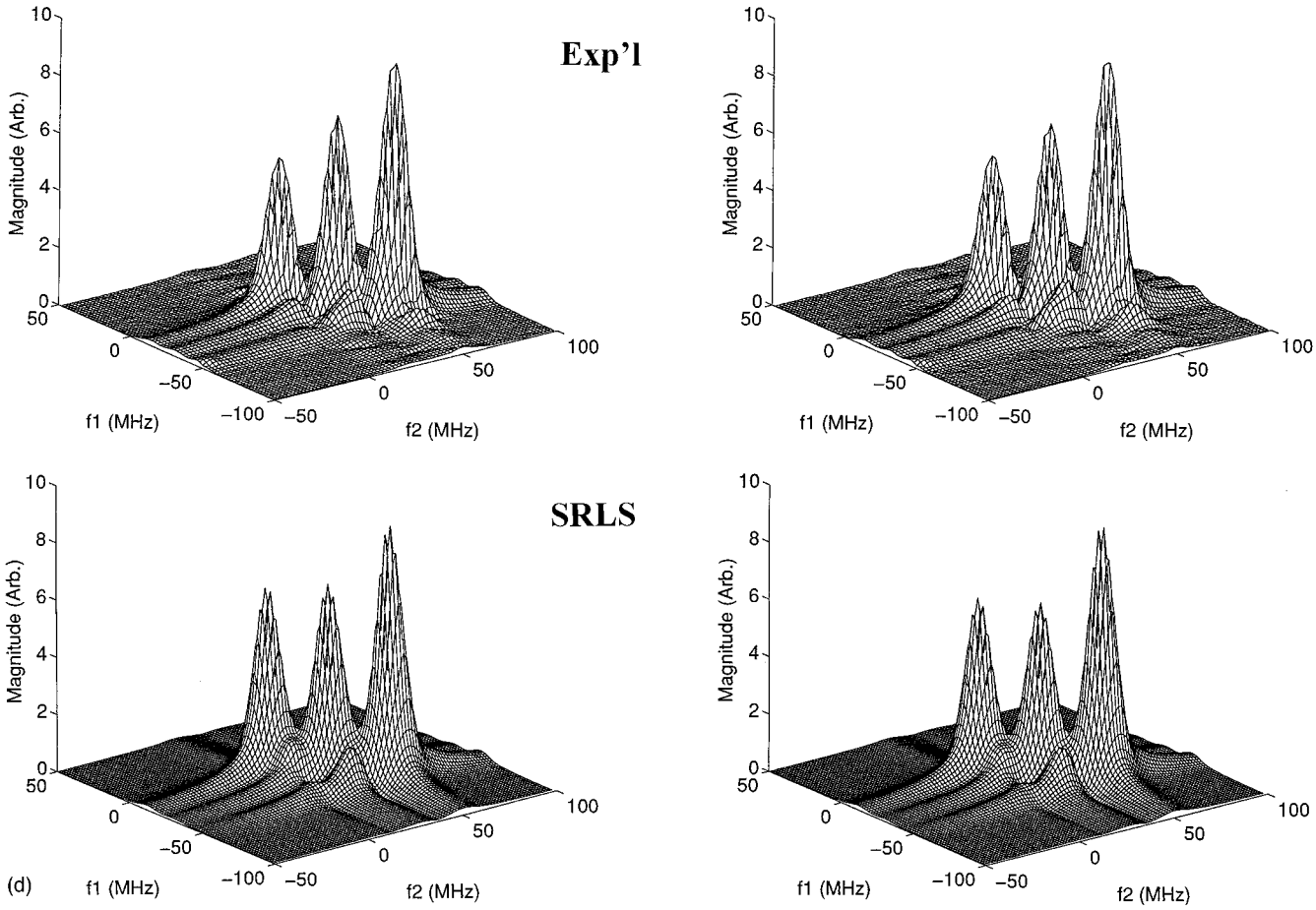

FIG. 3(d). See caption to Fig. 3(a).

IV. RESULTS

The magnitude 2D-ELDOR spectra that we have obtained over a range of temperatures including the isotropic (I), nematic (N), smectic A (S_A), smectic B (S_B), and crystal (C) phases and over a range of mixing times, T_m are illustrated as stack plots in Fig. 3. For compactness we only show results for two different mixing times (rather than all six or eight obtained) at a given temperature, and we only display results for one representative temperature in each phase. All spectra shown in these phases correspond to the nematic director aligned along the dc magnetic field, [i.e., the Euler angles, $\mathbf{\Omega}_d$ in Eq. (6) are given by (0,0,0)]. In Figs. 3(a), 3(b), and 3(c) we show the 2D-ELDOR spectra for $T_m=110$ and 250 ns for the I, N, and S_A phases, respectively, and in Figs. 3(d) and 3(e) the spectra for the S_B and C phases respectively are for somewhat longer values of T_m. In each case one observes the cross-peaks growing in as T_m increases. This is clearest for the I, N, and S_A phases, which are the most fluid. The cross-peaks are weaker and develop more slowly for the S_B and C phases. In Fig. 4 the development of the cross-peaks can be followed for one temperature (59 °C) in the S_A phase in a contour plot. Also, in Fig. 5 the different behavior in the five phases is compared with contour plots all obtained at the same mixing time of $T_m=200$ ns. One sees a large difference between the I phase and the ordered phases as the macroscopic alignment confines the 2D-spectra to a smaller region of frequencies. This compression is largest in the S_A, S_B, and C phases. The weaker development of the cross-peaks in the S_B and C phases is also evident.

In the S_A and S_B phases we also conducted experiments as a function of orientation of the nematic director with respect to the dc magnetic field. Here, for each orientation, 6–8 mixing times were again studied. We show in Fig. 6 the progression of the 2D-ELDOR spectra obtained at 57 °C (S_A phase) with tilt angle Θ for $T_m=400$ ns. The pattern of auto and cross-peaks is seen to depend significantly upon Θ. This includes substantial variation in their location with respect to f_1 and f_2, as expected for a macroscopically aligned sample, and in the relative intensities of the cross-peaks. The cross-peaks reflect $2W_n$, the nuclear-spin-flip rate generated by the electron–nuclear dipolar interaction (i.e., the second term in Eq. (2)) and are expected to be strongly dependent upon Θ in macroscopically aligned phases.[3,7]

The 2D-ELDOR spectra for $\Theta=0$ were initially simulated by both the standard and SRLS models. In all the phases the simulated spectra based upon the SRLS model

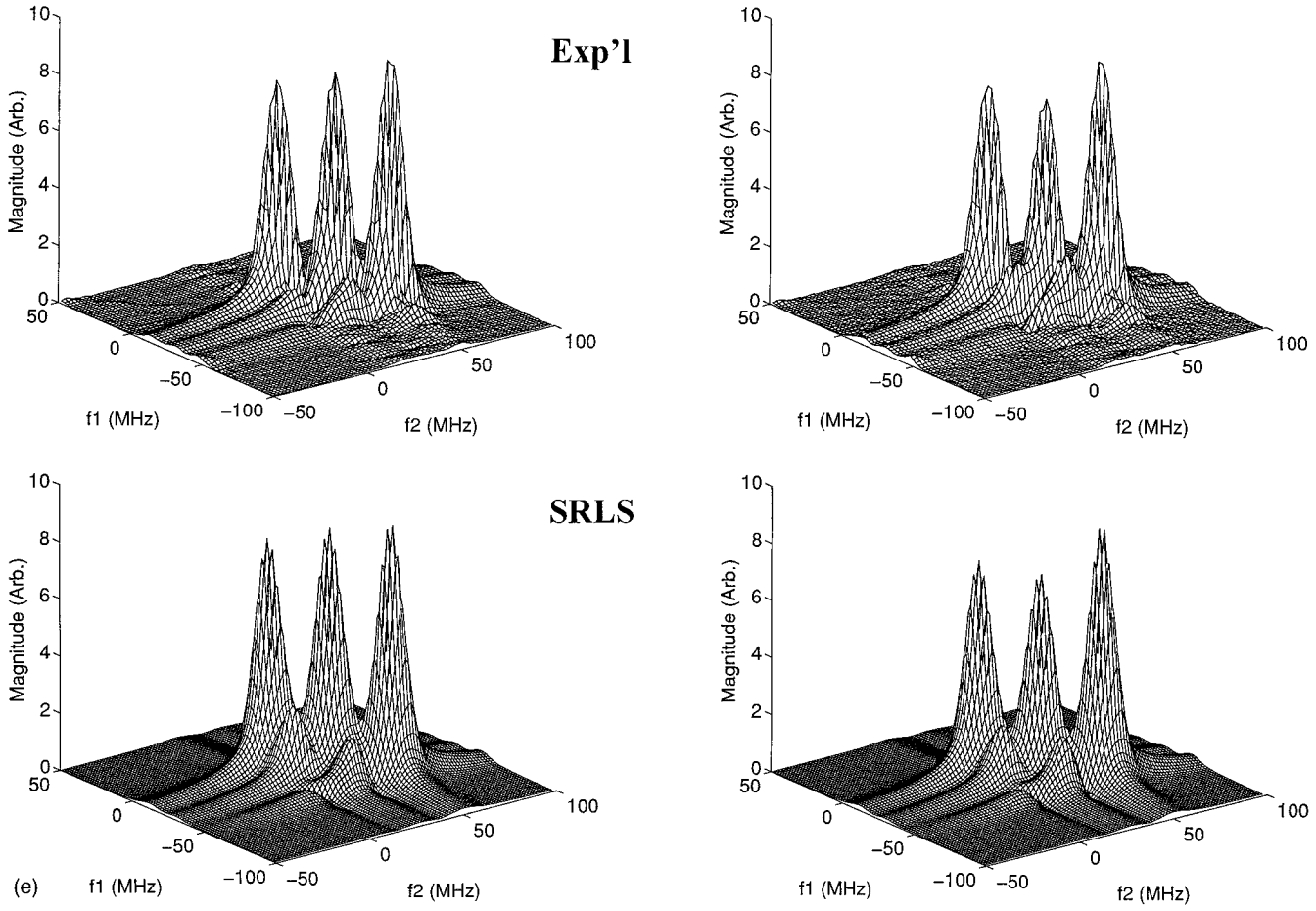

FIG. 3(e). See caption to Fig. 3(a).

were in better correspondence with experiment than was the standard model, and this difference became greater in the ordered phases. The final analyses were then performed by NLLS methods[21] simultaneously including all 6–8 mixing times at a given temperature. These complete NLLS fits were performed for the SRLS model for all the temperatures studied and for the standard model for representative temperatures in the I, N, and S_A phases. The best fitting parameters from these fits are presented in Table I, and associated simulations appear in Figs. 3 and 4. The evolution of the 2D-ELDOR spectra with T_m was found to play a very significant role in our comparison of the success of both models. Even for the I phase fits, one observes how the standard model requires the cross-peaks to develop too rapidly with mixing time, whereas their development is more correctly predicted by the SRLS model (cf. Fig. 3(a)). This is again true in the N phase (cf. Fig. 3(b)). Greater discrepancies between experiment and simulation with the standard model appear in Fig. 3(c) for the S_A phase, whereas quite good agreement is achieved with the SRLS model. This agreement is reinforced by the comparison of contour plots in Fig. 4. Figures 3(d) and 3(e) illustrate the fairly good agreement with the SRLS model obtained for the S_B and C phases. In our fits, we found that the ratio $N \equiv R_{\parallel}^{o}/R_{\perp}^{o}$ of the parallel and perpendicular rotational diffusion coefficients of the probe were about 6 in the I and N phases corresponding nearly to the ratio expected from Stokes–Einstein–Perrin considerations and the molecular geometry (i.e., 5, cf. Ref. 31). However, this was found not to be the case for the S_A, S_B, and C phases, which required a larger value of this ratio, of about 15–30. The simulations based on the standard model, on the other hand, led not only to poorer fits compared to the SRLS model for this phase (cf. Fig. 3(c)), but they also led to very high and unrealistic apparent values of N of over 200. Similar observations were made earlier by Meirovich and Freed[17] in their cw-ESR study of CSL in 4O,8 and other liquid crystal solvents.

We did not include the $\Theta \neq 0$ results in our analysis, because they led to exceedingly long times for the simulations. The reduced symmetry of the problem can increase the basis sets required by as much as an order of magnitude. In the lower temperature phases, we already required 60 to 70 hours of computer time to fit a set of $\Theta = 0$ 2D-ELDOR spectra at a single temperature. Thus the inclusion of $\Theta \neq 0$ spectra would have led to prohibitive times for the computations.

We present in Table I a listing of all the parameters obtained in our NLLS fits of the SRLS model to all the

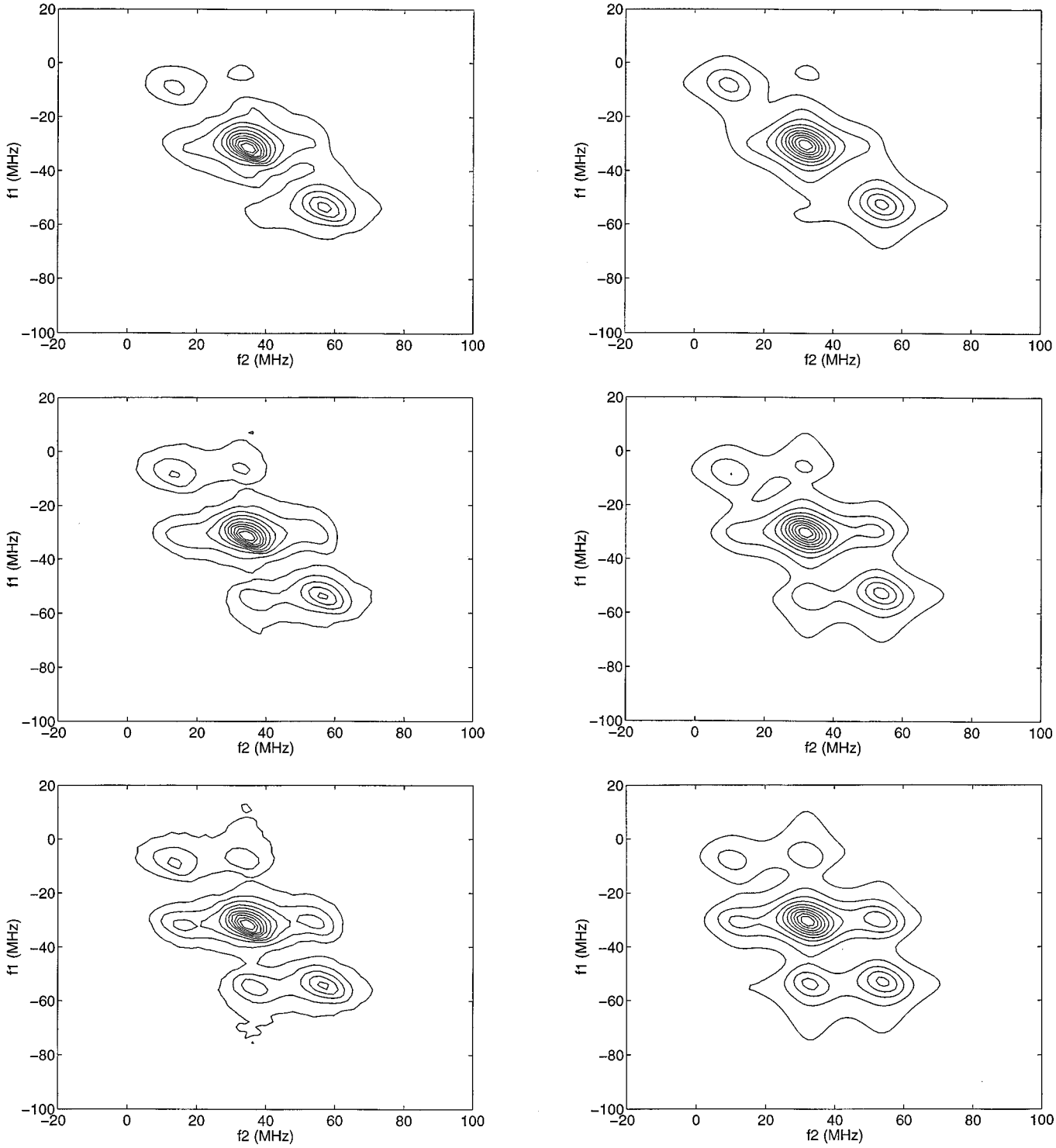

FIG. 4. Comparison of experimental (left column) and simulated (right column) 2D-ELDOR spectra (contour plots) based on SRLS model at 59 °C in the S_A phase. Upper, middle, and bottom rows correspond to $T_m = 90$ ns, 170 ns, and 250 ns, respectively.

spectra obtained for $\Theta = 0$. One notes the extensive number of parameters that are simultaneously obtained from these fits, 10 in all. In addition to $R_{\|}^{o}$ and $R_{\perp}^{o}$, the reorientational diffusion coefficient of the cage, R^{c}, is also obtained. These three diffusion coefficients are plotted vs T in Fig. 7. We also obtain the dimensionless potential coefficients a_0^2 and a_2^2, which appear in Eq. (10) and describe the (macroscopic) mean aligning potential experienced by the CSL in the ordered phases. They are plotted vs T in Fig. 8(a), and the resulting order parameters $S_0^2 = \langle \mathscr{D}_{0,0}^2(\mathbf{\Omega}^o) \rangle$ and $S_2^2 = \langle \mathscr{D}_{0,2}^2(\mathbf{\Omega}^o) + \mathscr{D}_{0,2}^2(\mathbf{\Omega}^o) \rangle$ obtained from Eq. (10) in the standard way, i.e.:

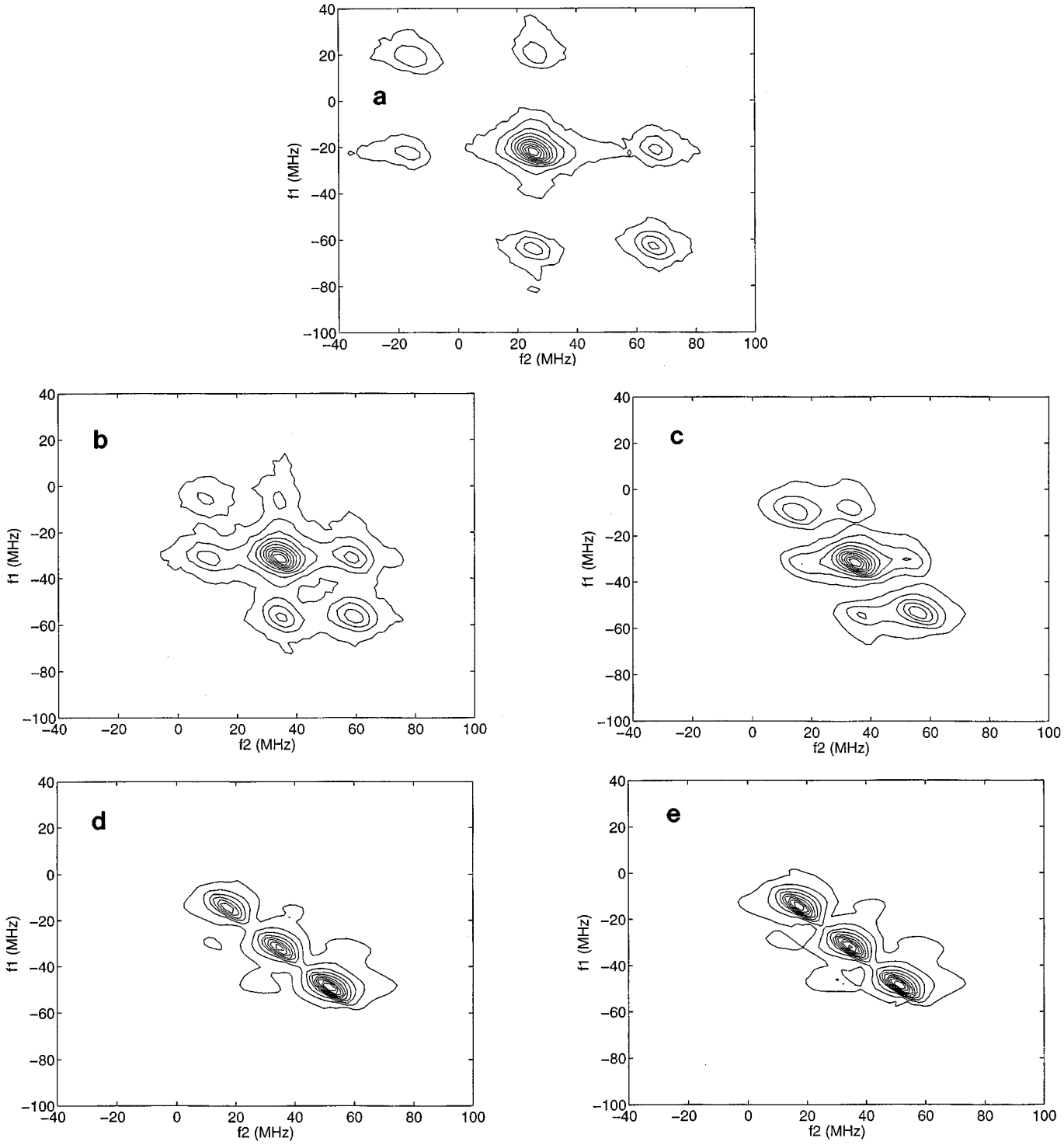

FIG. 5. Contour plots of experimental spectra at a fixed mixing time (200 ns), at representative temperatures in each of the phases: (a) isotropic, 91 °C; (b) nematic, 66 °C; (c) smectic A, 56 °C; (d) smectic B, 41 °C; (e) crystal, 29 °C.

$$\langle \mathscr{D}^L_{OK}(\mathbf{\Omega}^o)\rangle = \int d\mathbf{\Omega}^o \mathscr{D}^L_{DK}(\mathbf{\Omega}^o)\exp[-v^o(\mathbf{\Omega}^o)] \Big/ \int d\mathbf{\Omega}^o \times \exp[-v^o(\mathbf{\Omega}^o)] \tag{43}$$

are shown in Fig. 8(b). The dimensionless coefficients c_0^2 and c_2^2, which appear in Eq. (12) and describe the potential of interaction of the probe in the cage, are also obtained. They are plotted vs T in Fig. 9(a), and the resulting local order parameters $S^2_{l,0}=\langle \mathscr{D}^2_{0,0}(\mathbf{\Omega})\rangle$ and $S^2_{l,2}=\langle \mathscr{D}^2_{0,2}(\mathbf{\Omega}) + \mathscr{D}^2_{0-2}(\mathbf{\Omega})\rangle$ given by:

TABLE I. Optimum parameters obtained from fits to the SRLS model.[a]

Phase	T (°C)	$R_{\parallel}^{o}\times10^{-9}$ (s^{-1})	$R_{\perp}^{o}\times10^{-9}$ (s^{-1})	a_0^2	a_2^2	$T_{1,e}\times10^{6}$ (s)	$T_{2,e}\times10^{6}$ (s)	Δ_G (G)	c_0^2	c_2^2	$R^c\times10^{-7}$ (s^{-1})
I	96.2	0.62	0.119	⋯	⋯	0.068	0.135	1.12	1.10	0.96	2.03
I	91.0	0.57	0.094	⋯	⋯	0.077	0.152	1.07	1.04	0.95	0.90
I	86.1	0.53	0.088	⋯	⋯	0.072	0.188	1.15	0.69	1.00	0.43
I	80.2	0.49	0.080	⋯	⋯	0.110	0.187	1.02	0.73	0.96	0.48
N	73.1	0.77	0.138	1.93	1.46	0.582	0.095	0.86	1.85	0.62	1.08
N	70.2	0.68	0.131	2.15	0.86	0.582	0.111	0.93	2.00	0.62	1.40
N	67.5	0.65	0.121	2.50	1.12	0.582	0.122	0.82	1.84	0.81	1.01
N	65.0	0.54	0.101	2.74	1.27	0.582	0.138	0.80	1.72	0.62	0.84
S_A	59.1	2.37	0.081	3.57	0.84	0.288	0.283	0.94	2.26	0.82	0.33
S_A	56.4	2.36	0.086	3.79	1.16	0.359	0.343	1.01	2.23	0.78	0.32
S_A	53.6	2.48	0.077	4.15	1.44	0.478	0.442	1.11	2.25	0.79	0.33
S_A	50.8	2.33	0.083	4.68	1.17	0.316	0.196	1.28	1.62	0.74	0.28
S_B	44.4	3.23	0.150	7.49	−0.62	0.185	0.092	1.19	0.215	−0.029	0.022
S_B	40.7	2.86	0.115	7.78	−0.50	0.178	0.098	1.19	0.191	−0.003	0.021
S_B	38.1	2.77	0.150	7.55	−0.58	0.206	0.095	1.21	0.246	−0.010	0.022
S_B	35.2	2.09	0.141	7.62	−0.88	0.216	0.103	1.23	0.451	−0.027	0.015
C	29.1	2.00	0.124	7.61	−0.86	0.216	0.108	1.23	0.200	−0.004	0.010
C	24.6	1.98	0.137	7.96	−1.40	0.216	0.116	1.23	0.075	−0.002	0.000

[a]The average percent errors to the parameters are $\epsilon_{R_{\parallel}^{0}}=1.5$, $\epsilon_{R_{\perp}^{0}}=2.7$, $\epsilon_{a_0^2}=1.8$, $\epsilon_{a_2^2}=1.1$, $\epsilon_{T_{1,e}}=2.5$, $\epsilon_{T_{2,e}}=5.0$, $\epsilon_{\Delta_G}=1.6$, $\epsilon_{c_0^2}=2.5$, $\epsilon_{c_2^2}=2.7$, $\epsilon_{R^c}=3.7$.

$$\langle \mathscr{D}_{OK}^{L}(\mathbf{\Omega})\rangle = \int d\mathbf{\Omega}\mathscr{D}_{OK}^{L}(\mathbf{\Omega})\exp[-v^{\mathrm{int}}(\mathbf{\Omega})]\Big/\int d\mathbf{\Omega}\times\exp[-v^{\mathrm{int}}(\mathbf{\Omega})] \tag{44}$$

appear in Fig. 9(b). These are the principal parameters of interest in the present work. The additional parameters that were fit are (i) $T_{1,e}$, the electron-spin longitudinal relaxation time; (ii) $T_{2,e}^{-1}$ which includes additional contributions to the homogeneous linewidth not produced by the rotational modulation of the hf and g-tensor terms in Eq. (3), such as spin-rotational relaxation and intramolecular dipolar interactions between the electron spin and the CSL and solvent protons;[32] (iii) Δ_G, the inhomogeneous contribution to the linewidths assumed to be Gaussian.[6,21] Note that Δ_G shows only small variation with phase as expected. One expects that $T_{2,e}\leqslant T_{1,e}$ from general considerations.[7,33] We find that our results are consistent with this inequality for all the ordered phases. In the isotropic phase it would appear that $T_{1,e}$ is shorter than the $T_{2,e}$ from the additional linewidth contributions. Note, however that the $(T_{1,e}^{-1}-T_{2,e}^{-1})\approx 5\times10^{6}$ s^{-1} corresponds to about 0.3 G ''missing'' line broadening. We do find that the fits to $T_{2,e}$ and Δ_G correlate somewhat,[5] whereas $T_{1,e}$ is independently determined after fitting the other parameters. We believe that this corresponds to a small overestimate of Δ_G and a corresponding underestimate of $T_{2,e}^{-1}$ obtained for this phase. A similar defect shows up for this phase using fits to the standard model, cf. Table II.

The diffusion coefficients shown in Fig. 7 exhibit somewhat interesting behavior. $R_{\perp}^{o}$ is found to remain at about 10^{8} s^{-1} over the observed temperature range. There is some slowing down with decrease in temperature in the I and N phases. There is essentially no temperature variation in the S_A phase, but there is a small increase in the S_B phase. $R_{\parallel}^{o}$, which is about 6×10^{8} s^{-1} in the I and N phases, shows similar behavior, except for its substantial increase in the S_A phase compared to the N nematic phase, which yields the increased rotational anisotropy noted above. R^c is of order 10^{7} s^{-1} in the I and N phases and is thus substantially slower than $R_{\perp}^{o}$ or $R_{\parallel}^{o}$ as one would expect. It decreases in both phases with a decrease in T (except near the I–N phase transition), while it remains practically constant in the S_A phase. The onset of the S_B phase brings about a large drop in R^c to about 10^{5} s^{-1} signaling an abrupt freezing of the cage.

In Fig. 8(a) we see that the mean field potential a_0^2 shows a steady increase through the N and S_A phases, which is the generally expected behavior. However, there is a sudden large increase in a_0^2 with the onset of the S_B phase. The non-axial potential term a_2^2 is seen to drop practically to zero in the S_B phase. [These features are mirrored in the behavior of the order parameters in Fig. 8(b).] The cage potential parameters show a very interesting and contrasting behavior in this context. The axial parameter, c_0^2, which is small but significant in the I phase, increases substantially in the N phase, with a faster increase in the S_A phase, but abruptly dropping almost to zero in the S_B phase, signifying that the

TABLE II. Optimum parameters obtained from fits to the standard model.

Phase	T (°C)	$R_{\parallel}^{o}\times10^{-10}$ (s^{-1})	$R_{\perp}^{o}\times10^{-9}$ (s^{-1})	a_0^2	a_2^2	$T_{1,e}\times10^{6}$ (s)	$T_{2,e}\times10^{6}$ (s)	Δ_G (G)
I	91	0.208	0.037	⋯	⋯	0.073	0.23	1.0
N	65	0.180	0.026	2.67	−0.99	0.59	0.11	0.77
S_A	59	9.94	0.043	3.68	1.81	0.094	0.28	1.15

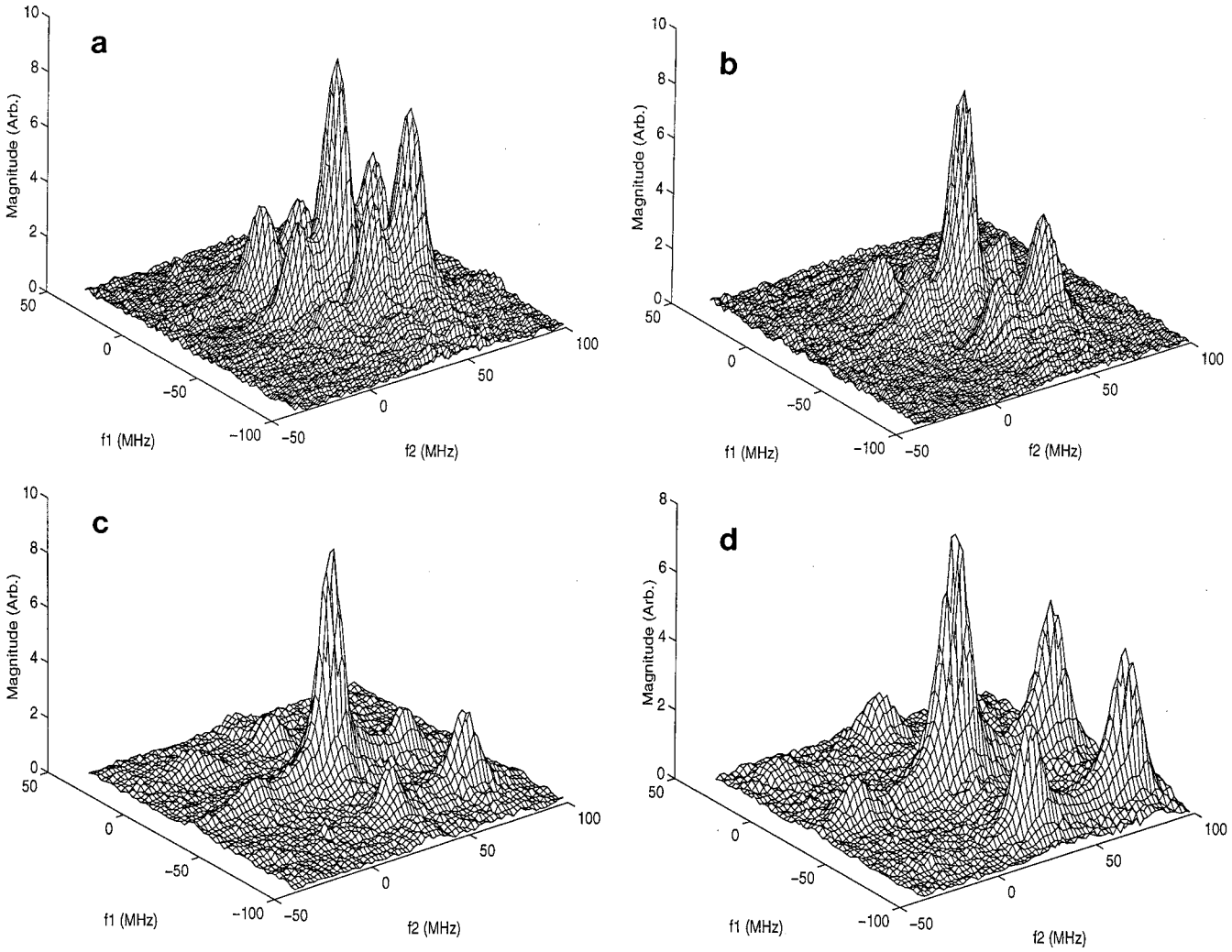

FIG. 6. Orientation dependence of experimental 2D-ELDOR spectra (stack plots) at 57 °C in the smectic A phase. All correspond to a $T_m = 400$ ns: (a) 0°; (b) 15°; (c) 45°; (d) 90°.

probe is hardly sensing a cage on the formation of the S_B phase. The non-axial coefficient c_2^2 in fact goes to zero in the S_B phase. This decrease is concomitant with the increase in a_0^2 at the $S_A - S_B$ transition, and the large drop in R^c. All these observations imply a freezing out of the cage so that its slowly fluctuating potential becomes an additive component of the mean field potential at this transition.

V. DISCUSSION

The most striking observation that emerges from our analysis of the 2D-ELDOR results on CSL in 4O,8 in terms of the SRLS model is the behavior at the $S_A - S_B$ transition. This is essentially a melting transition wherein the S_A phase is liquid-like, yet with orientational and translational order, but in the S_B phase the smectic layered structure is more frozen in to yield a hexagonal close-packed structure with strong interlayer correlations leading to three-dimensional positional ordering.[34] The principal motion that remains is molecular rotation about the long axis of the molecule (i.e., the $R_{\|}^o$ motion), with perhaps some wagging of the long axis within the very large orientational potential, which yields $S_0^2 \approx 1$. In fact, we find for CSL that $S_0^2 \approx 0.9$ and $S_2^2 \approx 0$ in the S_B phase with virtually identical ordering in the C phase. In the S_A phase we can still distinguish a dynamic cage affecting the CSL molecule in addition to the substantial macroscopic order $S_0^2 \approx 0.7$. This ''cage'' is presumably due to local regions of enhanced order as well as a collective wagging of the nearby liquid–crystal molecules. We may therefore expect that in the S_B phase this process freezes out leading to additional macroscopic alignment which is, of course, what we observe. The fact that our analysis predicts that the cage relaxes much more slowly and only has a residual effect on the CSL probe in the S_B and C phases, in accordance with expectation, is an encouraging result in support of our model in addition to the improved fits to experiment that we achieve.

We might expect additional improvements in the fits as we improve the SRLS model. The molecular dynamics results on an isotropic fluid showed that there should be some local variation in the magnitude of the cage orientational

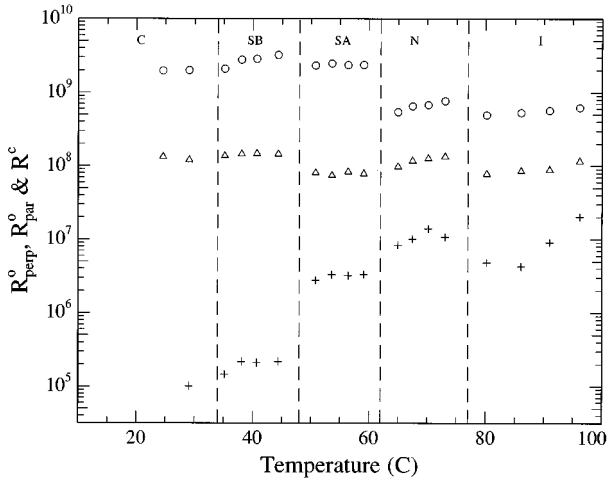

FIG. 7. Rotational diffusion coefficients for the probe: $R_\parallel^o$ (open circles) and $R_\perp^o$ (open triangles), as well as the cage (plus signs), plotted as a function of temperature.

potential,[22] although the dominant cage relaxation was in its reorientation. Thus one may introduce, as an additional relaxation process, time-dependent fluctuations in the magnitude of the coefficients c_0^2, c_2^2, etc. in Eq. (12). This might help in the fits to the *I* and *N* phases which show somewhat greater deviations. Additionally one could use higher order terms in the expansion of the cage potential [cf. Eq. (12)]. We discuss some other aspects of improved modeling in the second paper.[15]

In the original cw-ESR study of Meirovitch and Freed[17] on CSL in 4O,8 and related liquid crystalline solvents they reported on a large *apparent* anisotropy, *N* in the rotational diffusion tensor needed to fit the cw-ESR line shapes, especially in the smectic phases. Although they suggested a SRLS model as a way to explain the experiment, and the one they favored on physical grounds, they could not adequately test it for two reasons: (1) ''The intrinsic low sensitivity to the dynamics of the ESR spectra in this region of very high ordering and slow motion;'' and (2) no theory existed to describe its effects on slow motional spectra. In the present study we have been able to overcome limitation (1) by benefitting from the greatly enhanced sensitivity to motion of the 2D-ELDOR experiment, and modern computational algorithms[27,28,21] have made the challenging calculations of the SRLS model feasible even for simulating 2D-ELDOR. We do indeed find that more reasonable values of *N* are achieved once the SRLS model is introduced. It remains to be seen whether improvements in the model (e.g., see above) and the use of the orientation-dependent experimental spectra for the smectic phases will further modify the predicted values of *N*. Both will require more powerful algorithms or useful approximate methods to render the resulting computations more practical.

Another feature of the SRLS model compared to the standard model is the lower values of $R_\parallel^o$ and $R_\perp^o$ obtained with the latter (compare the results in Table II with those in Table I). This is most likely the result of fitting the cross-peak intensities which depend on W_n, the nuclear-spin flip rates generated by rotational modulation of the ^{14}N hf-tensor. Typically $W_n \propto (6R)^{-1}[1+(\omega_n/6R)^2]$ for simple isotropic Brownian motion [cf. Ref. 15] (with ω_n the nuclear-spin flip broadening of the auto-peaks vs T_m. We performed such an frequency), where $\omega_n \approx 2.6\times 10^8$ s^{-1} for CSL in the isotropic phase and $\omega_n \approx 2.0\times 10^8$ s^{-1} in the S_A phase. Thus, for typical values of $6R_\parallel^o \approx 3\times 10^9$ s^{-1} and $6R_\perp \approx 5\times 10^8$ in the *I* and *N* phases from the SRLS fit $W_n \tilde{\propto} (6R)^{-1}$ (actually a sum of contributions linear[7(a)] in $(R_\parallel^o)^{-1}$ and $(R_\perp^o)^{-1}$). In the absence of the contribution to W_n from the cage mechanism, the W_n predicted using the values of $R_\parallel^o$ and $R_\perp^o$ obtained from the SRLS fit would be too small, so one compensates by decreasing $R_\parallel^o$ and $R_\perp^o$

In the 2D-ELDOR studies on membrane vesicles using CSL, an interesting observation was made.[5] It is possible to convert the present COSY and COSY-based 2D-ELDOR S_C-spectra into SECSY format by replacing $t_2 \rightarrow t_1 + t_2$. After Fourier transforming with respect to the new t_2 variable, the exponential decays in t_1 lead to the homogeneous T_2 values. It was found in that work that the ''apparent'' T_2^{-1} values extracted from the 2D-ELDOR auto-peaks were increasing linearly with mixing time, T_m. Since the true T_2 cannot vary with mixing time, it was suggested that this could be a manifestation of collective director fluctuations, which are too slow and too small to significantly affect cw-ESR linewidths (cf. Sec. I). However, in 2D-ELDOR one has the potential to observe the ''real-time motion'' of a spin label as it adjusts to the director orientation Θ slowly changing to a new orientation Θ', or else as the label diffuses into a region with director orientation Θ'. Because this mechanism leads to a slight change in the ESR resonant frequency, exchange cross-peaks appear as an apparent increase in the analysis of the ''homogeneous width'' of the central auto-peak ($M_s=0$) obtained along the f_1-axis (for $f_2=0$) from the SECSY format for several temperatures, and we did not see any variation. Its absence in the present study could be for several reasons. In the present study we typically went to a maximum T_m of 300 ns compared to 2 μs in the study of membrane vesicles. (This was partly the result of the shorter values of T_{1e} in the present experiments, which limits the maximum value of T_m.) This may be insufficient time to observe the effects, so μs times might well be needed to see significant effects. However, another question is whether the (non-Markovian) feature of the slow cage dynamics in the SRLS model would be capable of causing an apparent broadening of T_2^{-1} with mixing time. We performed simulations of the SECSY-type of 2D-ELDOR experiment, using the parameters from Table I that were obtained from the fit to the 53.6 °C S_A phase experiments. Here $R^c = 3.3\times 10^6$ s^{-1} corresponding to a reorientational correlation time of $\tau_R^c = 50$ ns. Over the experimentally studied range of $T_m = 90$ to 250 ns no variation of the central auto-peak is predicted, consistent with experiment. One might expect to see slow cage dynamics in the S_B phase where $R^c = 2\times 10^5$ s^{-1} ($\tau_R^c = 800$ ns), but

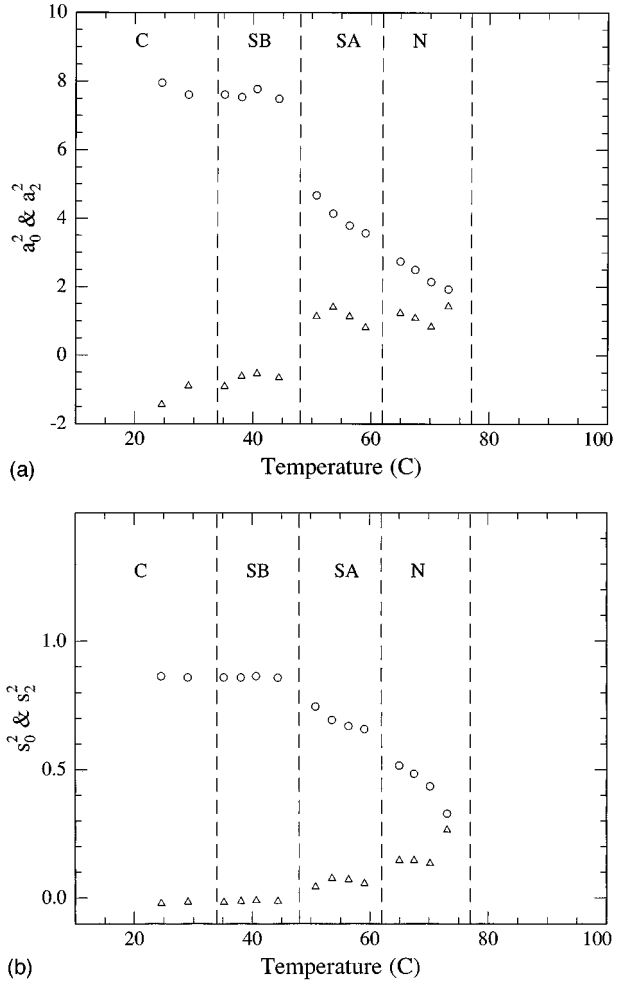

FIG. 8. (a) Mean field (macroscopic) orienting potential parameters: a_0^2 (open circles) and a_2^2 (open triangles), as a function of temperature (from SRLS model simulations). (b) Mean field (macroscopic) order parameters: $S_0^2=\langle \mathscr{D}_{00}^2 \rangle$ (open circles) and $S_2^2=\langle \mathscr{D}_{02}^2+\mathscr{D}_{0-1}^2 \rangle$ (open triangles), as a function of temperature (from SRLS model simulations).

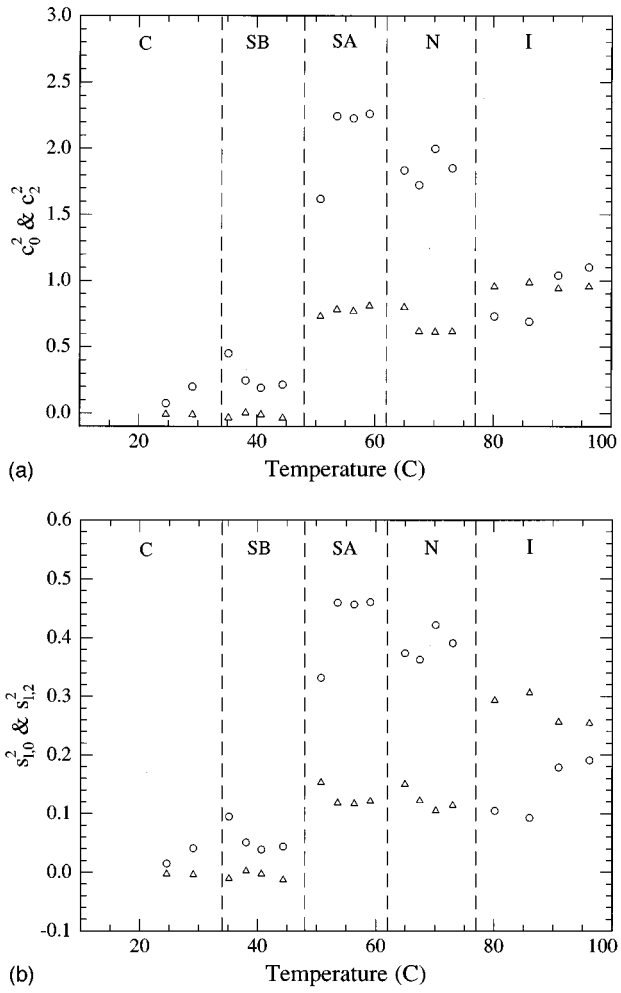

FIG. 9. Cage potential parameters: c_0^2 (open circles) and c_2^2 (open triangles), as a function of temperature (SRLS model simulations). (b) Cage order parameters: $S_{I,0}^2=\langle \mathscr{D}_{00}^2 \rangle_I$ (open circles) and $S_{I,2}^2=\langle \mathscr{D}_{20}^2+\mathscr{D}_{-20}^2 \rangle_I$ (open triangles), as a function of temperature (SRLS model simulations).

as discussed above the interaction potential [cf. Eq. (12)] is very weak in this phase.

In another context, however, there does appear to be an important similarity between the present 2D-ELDOR study of CSL in a macroscopically aligned liquid crystal and the study of CSL in membrane vesicles. A careful examination of the cross-peak development as a function of T_m in the vesicle study shows that this evolution is approximately predicted by the standard model, but it is not very accurate. There is more substantial variation with T_m that is observed experimentally than is predicted by the standard model. This is just the type of behavior that we have observed in the present work, which is better fit by a SRLS model. Thus, we may expect improved fits to 2D-ELDOR experiments on membranes by employing the SRLS model.

VI. CONCLUSIONS

This study has shown that 2D-ELDOR experiments as a function of mixing time are particularly sensitive to the motional dynamics of the CSL probe in a liquid crystalline solvent. Significant improvements in fitting to the 2D-ELDOR spectra are obtained by the use of the slowly relaxing local structure (SRLS) model to represent the effects of a dynamic cage on the reorientational motion of the CSL probe in the different liquid crystalline phases of 4O,8. The SRLS model provides a consistent picture of the motional dynamics, wherein the dynamic cage formed by the neighboring liquid crystal molecules is in addition to the static macroscopic mean field, and it has a time average of zero. This dynamic cage relaxes at least an order of magnitude slower than the rotational reorientation of the CSL in the combined potential. There is a modest cage potential in the isotropic phase (~ 1 k_BT) which jumps to 2–2.5 k_BT in the nematic phase, but drops to a very small value in the S_B and C phases. This drop in cage potential at the S_A-S_B transition is concomitant with an almost comparable increase in the static mean field potential consistent with the freezing in of the aligned structure in this phase.

ACKNOWLEDGMENTS

This work was supported by National Science Foundation Grants Nos. CHE93 13167 and DMR 9210638 and NIH Grants Nos. GM25862 and RR07126. A.P. acknowledges the support of the Italian Ministry for Universities and Scientific and Technological Research and thanks Professor P. L. Nordio and Professor G. J. Moro for enlightening discussions. The computations reported here were performed at the Cornell Theory Center.

[1] J. Gorcester and J.H. Freed, J. Chem. Phys. **85**, 5375 (1986).
[2] J. Gorcester and J.H. Freed, Chem. Phys. **88**, 4678 (1988).
[3] J. Gorcester, S.B. Rananavare, and J.H. Freed, J. Chem. Phys. **90**, 5764 (1989).
[4] S. Lee, B.R. Patyal, S. Saxena, R.H. Crepeau, and J.H. Freed, Chem. Phys. Lett. **211**, 397 (1994).
[5] R.H. Crepeau, S. Saxena, S. Lee, B.R. Patyal, and J.H. Freed, Biophys. J. **66**, 1489 (1994).
[6] S. Lee, D.E. Budil, and J.H. Freed, J. Chem. Phys. **101**, 5529 (1994).
[7] (a) J.H. Freed, A. Nayeem, and S.B. Rananavare, in *The Molecular Dynamics of Liquid Crystals*, edited by G.R. Luckhurst and C.A. Veracini (Kluwer, Dordrecht, 1994), Chap. 12; (b) J.H. Freed, A. Nayeem, and S.B. Rananavare, *ibid.*, Chap 15.
[8] (a) R.R. Vold and R.L. Vold, in Ref. 7, Chap. 9; (b) F. Noack and K.H. Schweikert, *ibid.*, Chap. 10.
[9] C.F. Polnaszek and J.H. Freed, J. Phys. Chem. **79**, 2283 (1975).
[10] J.H. Freed, A. Nayeem, and S.B. Rananavare, in Ref. 7, Chap. 14.
[11] A. Nayeem, S.B. Rananavare, V.S.S. Sastry, and J.H. Freed, J. Chem. Phys. **96**, 3912 (1992).
[12] R.Y. Dong, M. Wiszniewska, E. Tomchuck, and E. Bock, Can. J. Phys. **52**, 766 (1974); **53**, 610 (1975).
[13] G. Moro and P.L. Nordio, J. Phys. Chem. **89**, 997 (1985).
[14] J.K. Moscicki, Y.K. Shin, and J.H. Freed, J. Chem. Phys. **99**, 634 (1993).
[15] V.S.S. Sastry, A. Polimeno, R.H. Crepeau, and J.H. Freed, following paper, J. Chem. Phys. **105**, 5773 (1996).
[16] T.B. Marriott, G.B. Birrell, and O.H. Griffith, J. Am. Chem. Soc. **97**, 627 (1975).
[17] E. Meirovitch and J.H. Freed, J. Phys. Chem. **84**, 2459 (1980).
[18] L. Kar, E. Ney-Igner, and J.H. Freed, Biophys. J. **48**, 569 (1985).
[19] J.H. Freed, A. Nayeem, and S.B. Rananavare, in Ref. 7, Chap. 13.
[20] A. Polimeno and J.H. Freed, J. Phys. Chem. **99**, 10995 (1995).
[21] D.E. Budil, S. Lee, S. Saxena, and J.H. Freed, J. Magn. Res. **A120**, 155 (1996).
[22] A. Polimeno, G. Moro, and J.H. Freed, J. Chem. Phys. **102**, 8094 (1995); **104**, 1090 (1996).
[23] C.W. Garland, M. Meichle, B.M. Ocko, A.R. Kortan, C.R. Safinya, L.J. Yu, J.D. Litster, and R.J. Birgeneau, Phys. Rev. A **27**, 3234 (1983).
[24] J. Gorcester, G.L. Millhauser, and J.H. Freed, in *Modern Pulsed and Continuous Wave Electron Spin Resonance*, edited by L. Kevan and M.K. Bowman (Wiley, New York, 1990).
[25] S. Lee, B. Patyal, and J.H. Freed, J. Chem. Phys. **98**, 3665 (1993).
[26] E. Meirovitch and J.H. Freed, J. Phys. Chem. **88**, 4995 (1984).
[27] (a) D.J. Schneider and J.H. Freed, Adv. Chem. Phys. **73**, 387 (1989); (b) in *Biological Magnetic Resonance*, edited by L.J. Berliner and J. Reuben (Plenum, New York, 1989), Vol. 8, p. 1.
[28] (a) G. Moro and J.H. Freed, J. Chem. Phys. **74**, 3757 (1981); (b) in *Large Scale Eigenvalue Problems*, edited by J. Cullum and R.A. Willoughby (North-Holland, Amsterdam, 1986).
[29] E. Meirovitch, D. Igner, G. Moro, and J.H. Freed, J. Chem. Phys. **77**, 3915 (1982).
[30] K.V. Vasavada, D.S. Schneider, and J.H. Freed, J. Chem. Phys. **86**, 647 (1987).
[31] K.A. Earle, D.E. Budil, and J.H. Freed, J. Phys. Chem. **97**, 13289 (1993).
[32] J.S. Hwang, R.P. Mason, L.P. Hwang, and J.H. Freed, J. Phys. Chem. **79**, 489 (1975).
[33] A. Abragam, *The Principles of Nuclear Magnetism* (Oxford University Press, New York, 1961).
[34] (a) P.A.C. Gane, A.J. Leadbetter, and P.G. Wrighton, Mol. Cryst. Liq. Cryst. **66**, 247 (1981); (b) P.S. Pershan, G. Aeppli, J.A. Litster, and R.J. Birgeneau, *ibid.* **67**, 205 (1981).